

1
2
3
4
5
6
7
8
9
10
11
12
13
14
15
16
17
18
19
20
21
22
23
24
25
26
27
28
29
30
31

**From mantle peridotites to hybrid troctolites:
textural and chemical evolution during melt-rock interaction history
(Mt.Maggiore, Corsica, France)**

**Basch, Valentin¹; Rampone, Elisabetta¹; Crispini, Laura¹; Ferrando, Carlotta²;
Ildefonse, Benoit²; Godard, Marguerite²**

<http://dx.doi.org/10.1016/j.lithos.2018.02.025>

¹DISTAV, University of Genova, Corso Europa 26, I-16132 Genova, Italy

²Géosciences Montpellier, University of Montpellier, CNRS, Montpellier, France.

Corresponding Author:

Basch Valentin

Dipartimento di Scienze della Terra, dell' Ambiente e della Vita (DISTAV)
Università degli Studi di Genova
Corso Europa 26
I-16132 Genova (Italy)

Email: valentin.basch@gmail.com

32 **Abstract**

33 Recent studies investigate the replacive formation of hybrid troctolites from mantle
34 peridotites after multiple stages of melt-rock reaction. However, these studies are not
35 conducted in a field-controlled geological setting displaying the clear evolution from the
36 protolith to the end-product of the reactions. The Mt.Maggiore peridotitic body exposes a
37 clear evolution from spinel lherzolite to plagioclase-bearing lithotypes (plagioclase
38 peridotites, olivine-rich troctolites and troctolites) during two distinct episodes of melt-rock
39 interaction. In the spinel facies, the reactive percolation of a LREE-depleted melt leads to the
40 dissolution of mantle pyroxenes and the growth of olivine crystals, forming replacive spinel
41 dunites. The progressive evolution from spinel lherzolite to harzburgite to replacive dunite is
42 accompanied by a change of olivine Crystallographic Preferred Orientation (CPO), from
43 axial-[100] in the lherzolite to axial-[010] olivine CPO in the dunites, indicative of
44 deformation in presence of melt. The initial percolating melt composition is consistent with
45 single melt increments after 6% partial melting of a depleted mantle source. Reactive melt
46 percolation leads to a progressive enrichment in the melt M-HREE absolute concentrations,
47 while preserving its LREE depletion, consistent with the enriched analyzed HREE
48 composition of olivine in the spinel dunite.

49 In the shallower plagioclase facies, the melts modified by reactive melt percolation
50 impregnate the spinel-facies lithotypes, leading to the dissolution of olivine and
51 crystallization of plagioclase and orthopyroxene in the peridotites. This impregnation stage is
52 also observed in the spinel dunites, forming hybrid olivine-rich troctolites and troctolites. The
53 dissolution-precipitation reactions forming hybrid troctolites cause a progressive textural
54 evolution of the olivine matrix, with the disruption of deformed coarse grains into
55 undeformed small rounded grains. This textural evolution is not accompanied by clear
56 changes in the olivine CPO, indicating low instantaneous melt/rock ratios during the
57 impregnation process. Olivine, plagioclase and clinopyroxene REE compositions analyzed in
58 troctolite fit a process of impregnation with a progressive closure of the porosity (at
59 decreasing melt mass), leading to the crystallization of trapped melt and REE enrichments
60 during the last crystallization increments.

61

62 **Keywords: Alpine ophiolites; Melt-rock interaction; Reactive porous flow; Melt**
63 **impregnation; Olivine texture; Olivine trace elements.**

64 **1. Introduction**

65 Many studies have highlighted the importance of melt-rock interactions in developing
66 structural and geochemical heterogeneities in peridotites at different mantle depths (e.g.,
67 [Dijkstra et al., 2001, 2003](#); [Lissenberg and Dick, 2008](#); [Soustelle et al., 2009, 2010, 2014](#);
68 [Collier and Kelemen, 2010](#); [Higgie and Tommasi, 2012, 2014](#); [Tursack and Liang, 2012](#);
69 [Saper and Liang, 2014](#); [Dygert et al., 2016](#); [Paquet et al., 2016](#); [Renna et al., 2016](#)).
70 Specifically, melt-rock reactions have been invoked as important rock-forming processes
71 acting in the upwelling mantle in extensional settings. In such geodynamic environments,
72 replacive spinel harzburgites and dunites have been inferred as the product of open-system
73 reactive melt percolation, driven by pyroxene dissolution and olivine crystallization at deep
74 (spinel-facies) mantle levels (e.g., [Kelemen et al., 1995a, b, 2000, 2007](#); [Dick et al., 2008,](#)
75 [2010](#); [Piccardo et al., 2007](#); [Rampone et al., 2008](#); [Rampone and Borghini, 2008](#); [Lambart et](#)
76 [al., 2009](#); [Liang et al., 2011](#); [Pirard et al., 2013](#); [Dygert et al., 2016](#)), whereas plagioclase-rich
77 peridotites, ubiquitously found in ophiolitic and oceanic settings, are widely thought to result
78 from melt impregnation at shallower (plagioclase-facies) mantle depths (e.g., [Dijkstra et al.,](#)
79 [2001, 2003](#); [Borghini et al., 2007](#); [Rampone and Borghini, 2008](#); [Tursack and Liang, 2012](#);
80 [Saper and Liang, 2014](#)).

81 Melt-rock interactions have also been increasingly invoked as key processes in the
82 formation and compositional evolution of the oceanic crust, from several lines of evidence:
83 (1) the study of chemical zoning and melt inclusions in lava phenocrysts ([Laubier et al.,](#)
84 [2014](#); [Coumans et al., 2016](#)), (2) peculiar compositional trends observed in mid-ocean ridge
85 basalts (MORBs), not consistent with a process of pure fractional crystallization ([Collier and](#)
86 [Kelemen, 2010](#); [Van den Bleeken, 2011](#); [Paquet et al., 2016](#)), (3) olivine-rich troctolites
87 found enclosed in the lowermost oceanic crust, thought to represent the “hybrid” reactive
88 product of the interaction between dunites from the crust-mantle boundary and percolating
89 MORB melts, dissolving olivine and crystallizing interstitial plagioclase and clinopyroxene
90 ([Lissenberg and Dick, 2008](#); [Suhr et al., 2008](#); [Drouin et al., 2009, 2010](#); [Renna and Tribuzio,](#)
91 [2011](#); [Sanfilippo and Tribuzio, 2013](#); [Higgie and Tommasi, 2012](#); [Sanfilippo et al., 2013,](#)
92 [2014, 2015, 2016](#); [Rampone et al., 2016](#)). These latter studies have thus inferred the possible
93 incorporation of mantle slivers into the lower oceanic crust at slow-spreading ridges through
94 multiple melt-rock interaction episodes leading to the replacive formation of dunites, olivine-
95 rich troctolites and troctolites from mantle peridotites. However, the mantle origin of the
96 dunitic matrix and the resulting hybrid origin of troctolites (i.e., by dunite melt impregnation

97 rather than by fractional crystallization of a primitive melt) is difficult to demonstrate without
98 documenting the evolution from mantle peridotite protolith to the hybrid end-product.

99 The Alpine-Apennine ophiolites are predominantly constituted by mantle peridotites
100 and represent analogues of the oceanic lithosphere formed at ocean/continent transition and
101 slow- to ultra-slow spreading settings (Rampone et al., 1997, 2004, 2008; Rampone and
102 Piccardo, 2000; Müntener and Piccardo, 2003; Müntener et al., 2004; Piccardo et al., 2004;
103 Borghini et al., 2007; Manatschal and Müntener, 2009). Previous studies have documented
104 that many Alpine-Apennine peridotites record various stages of melt-rock interaction, which
105 occurred at different lithospheric levels during the extensional mantle exhumation (e.g.
106 Rampone and Borghini, 2008; Piccardo and Guarnieri, 2010).

107 The Mt.Maggiore (Alpine Corsica) peridotitic body displays lithological variations
108 clearly related to two episodes of melt-rock interaction: a first reactive melt percolation event
109 at spinel-facies, leading to the replacive formation of harzburgites and dunites, followed by
110 melt impregnation of the spinel peridotites and dunites at plagioclase-facies, crystallizing
111 plagioclase \pm orthopyroxene, and dissolving olivine (Jackson and Ohnenstetter, 1981;
112 Rampone et al., 1997, 2008; Müntener and Piccardo, 2003; Piccardo and Guarnieri, 2010).
113 Previous studies report a first spinel-facies reactive melt percolation in the spinel peridotites,
114 leading to the replacive formation of dunites (Rampone et al., 1997, 2008; Müntener and
115 Piccardo, 2003; Piccardo and Guarnieri, 2010). It is followed by a melt impregnation of the
116 spinel peridotites and dunites at plagioclase-facies, crystallizing plagioclase \pm orthopyroxene,
117 and dissolving olivine. In the field, the primary association between spinel- and plagioclase-
118 peridotites, dunites, and olivine-rich troctolites is preserved, and the replacive formation of
119 plagioclase peridotites and troctolites from the spinel-facies lithotypes during the melt
120 impregnation stage is therefore clearly recognizable. The Mt.Maggiore peridotitic body is
121 thus an ideal case study to investigate the structural and geochemical evolution of a mantle
122 peridotite protolith during the multiple melt-rock interaction stages leading to the replacive
123 formation of hybrid troctolites.

124 In this paper, we present new field mapping, coupled with Electron Backscattered
125 Diffraction (EBSD) measurements, and mineral major and trace elements analyses (by
126 Electron Probe Micro-Analyses (EPMA) and Laser Ablation-Inductively Coupled Plasma-
127 Mass Spectrometry (LA-ICP-MS), respectively) of Mt.Maggiore spinel and plagioclase
128 peridotites, spinel dunites, and troctolites, which aim at documenting and discussing the
129 textural and mineral chemical changes during formation of hybrid troctolites. We focus
130 specifically on combined textural observations (EBSD mapping) and trace element

131 geochemistry of olivine. Olivine is the major constituent in peridotites and troctolites, and is
132 extensively involved in the melt-rock reactions described in the oceanic lithosphere.
133 Although the behaviour of many trace elements in olivine is still poorly understood, recent
134 studies outlined the potential of olivine minor and trace elements in the investigation of
135 mantle processes, from melting to melt-rock interactions (e.g., [Drouin et al., 2009](#); [De Hoog](#)
136 [et al., 2010](#); [Foley et al., 2013](#); [Lissenberg et al., 2013](#); [Sanfilippo et al., 2014](#); [D’Errico et al.,](#)
137 [2016](#); [Rampone et al., 2016](#)).

138 Here we show that the trace element composition of olivine, coupled to EBSD
139 analyses, on a field-controlled sample set, constitute a powerful approach to investigate melt-
140 rock reaction processes leading to the origin of hybrid troctolites. Major outcomes of this
141 work are the demonstrated and quantified textural evolution of the olivine matrix during the
142 replacive formation of hybrid troctolites, and the evidence for microstructural and
143 geochemical inheritance of olivine in the troctolites from both dunite-forming and troctolite-
144 forming melt-rock interaction stages.

145

146 **2. Structural and petrologic background**

147 The Corsican mafic-ultramafic bodies are part of the Alpine-Apennine ophiolites,
148 thought to represent the lithosphere remnants of the narrow Jurassic Ligurian Tethys basin
149 (400-500 km) opened by passive lithosphere extension leading to slow- to ultra-slow
150 spreading oceanization ([Rampone & Piccardo, 2000](#); [Manatschal & Müntener, 2009](#)). The
151 Mt. Maggiore peridotitic massif has been interpreted as the deepest part of the reconstructed
152 “Schistes Lustrés” ophiolitic sequence, exposed in the eastern Alpine Corsica ([Fig. 1](#))
153 ([Jackson & Ohnenstetter, 1981](#)). Although it lacks any crustal cover, it preserves clear field
154 relationships between the mantle peridotites and associated pyroxenite and gabbroic
155 lithotypes. Previous studies showed that the peridotitic body records a multi-stage
156 lithospheric exhumation history, through various episodes of melt-rock interaction from deep
157 (spinel-facies) to shallower levels (plagioclase-facies) ([Rampone et al., 1997, 2008](#); [Müntener](#)
158 [& Piccardo, 2003](#); [Piccardo & Guarnieri, 2010](#)).

159 A first event of olivine-saturated reactive melt percolation leads to the dissolution of
160 mantle clinopyroxene and orthopyroxene, and crystallization of olivine at spinel facies
161 conditions. This melt-rock interaction is recorded in the spinel lherzolites and harzburgites by
162 the development of olivine embayments partly replacing mantle orthopyroxene and
163 clinopyroxene. Extensive reactive melt percolation is observed with the replacive formation

164 of spinel dunite pods and the partial to complete dissolution of pyroxenite layers primarily
165 associated with the spinel peridotites. In the clinopyroxene-poor spinel lherzolites and
166 harzburgites, the trace element compositions of clinopyroxenes are relatively homogeneous
167 and LREE depleted, consistent with residual mantle after low-degrees (5-8%) of fractional
168 melting (Rampone et al., 1997, 2008).

169 In the field, the Mt.Maggiore spinel peridotites grade to plagioclase-bearing
170 peridotites showing microstructural characteristics indicative of a plagioclase- (\pm opx)
171 crystallizing, olivine-dissolving melt impregnation (Rampone et al., 1997, 2008; Müntener &
172 Piccardo, 2003; Piccardo & Guarnieri, 2010). Highly impregnated plagioclase peridotites
173 often display plagioclase-rich gabbronoritic veinlets, crystallized after segregation of the
174 percolating melts. Rock-forming minerals in the gabbronoritic veinlets also show LREE
175 depleted patterns, indicating the depleted signature of the impregnating melts, which thus do
176 not correspond to an aggregated MORB (Rampone et al., 2008).

177 Together, the reported melt-rock interaction processes suggest the open-system
178 reactive percolation of an olivine-saturated depleted melt at spinel facies levels followed by
179 impregnation of the peridotites by migrating melts at shallower, colder lithospheric depths.
180 Rampone et al. (2008) described the progressive modification of the percolating melt
181 composition during the pyroxene-dissolving, olivine-crystallizing reactive melt percolation.
182 They inferred that melt-rock interaction occurring at spinel-facies led to a progressive
183 decrease in the olivine saturation and increase in pyroxene and plagioclase saturation.
184 Together with a change in lithospheric depth during upwards melt percolation (from spinel-
185 facies to plagioclase-facies), the compositional variations of the melt enabled an evolution in
186 the type of melt-rock interaction from an olivine-crystallizing, pyroxene-dissolving reactive
187 melt percolation at spinel-facies to a plagioclase \pm orthopyroxene \pm clinopyroxene melt
188 impregnation at plagioclase-facies. Both spinel and plagioclase peridotites were intruded by
189 later gabbroic dykes, ranging from olivine gabbros to diorites, showing a clear MORB-type
190 affinity (Piccardo and Guarnieri, 2010).

191

192 **3. Geology of the studied area**

193 We performed a detailed mapping of the Monte Maggiore peridotitic body and
194 merged our lithological and structural data with the already published data of Jackson and
195 Ohnenstetter (1981) in Fig. 1. The Mt.Maggiore peridotitic massif is mainly composed of
196 granular spinel and plagioclase peridotites, showing in places a weak foliation with a

197 preferential elongation of mantle pyroxenes (Fig. 1). The spinel peridotites show variations in
198 modal compositions, ranging from olivine-poor lherzolites (60% olivine) to olivine-rich
199 harzburgites (85% olivine) (Table 1). The mantle peridotites are primarily associated to
200 decimetre-size sub-vertical pyroxenite layers, showing a constant NW-SE orientation. In
201 places, these pyroxenite layers are partially dissolved. Similar sub-vertical NW-SE
202 orientations are reported for the foliation observed in the spinel peridotites. In places, the
203 spinel peridotites progressively grade to metre-size spinel dunitic bodies, through a diffuse to
204 sharp contact (Fig. 2a,b). The occurrence of aligned spinel trails within the dunite, indicative
205 of the former presence of a pyroxenite layer, in which pyroxenes were completely dissolved
206 (Fig. 2b), further evidences the replacive nature of the spinel dunites.

207 The spinel peridotites grade to plagioclase-bearing peridotites, showing an enrichment
208 in interstitial plagioclase and orthopyroxene. The most plagioclase-rich samples (up to 30%
209 interstitial minerals) show a steeply dipping (50-70°S) modal layering of plagioclase
210 enrichment, oriented ESE-WNW (Figs. 1, 3), and associated gabbroic veinlets (Fig. 2c).
211 The plagioclase peridotites are associated to bodies of olivine-rich troctolites and troctolites,
212 previously described as “cumulates” (Rampone et al., 1997; Müntener et al., 2003; Piccardo
213 and Guarnieri, 2010). Based on new field observations, we infer that these troctolitic bodies
214 correspond to the plagioclase-facies melt impregnation of the spinel dunites. At the
215 impregnation front, i.e. the transition from preserved spinel-bearing lithotypes to impregnated
216 plagioclase-bearing lithotypes, the spinel peridotite and associated dunite pods grade to
217 replacive plagioclase peridotite and troctolitic bodies, respectively. These troctolitic bodies
218 have variable modal compositions from 70 to 90% of granular olivine and up to 30% of
219 interstitial plagioclase (Fig. 2d,e). The most impregnated samples show a ESE-WNW
220 layering of plagioclase enrichment and formation of gabbroic veinlets, similar to what is
221 observed in the plagioclase peridotite (Figs. 1, 3). All spinel- and plagioclase-bearing
222 lithotypes and structures are crosscut by steeply dipping gabbroic dikes (60-80°S), trending
223 E-W to ESE-WNW (Figs. 1, 3).

224 At the scale of the massif, zones that preserve the primary evolution of mantle
225 peridotites and associated lithologies are separated by low-grade alteration zones rich in
226 serpentine veins (reported as *Serpentine veinlets-bearing peridotite* in Fig. 3). These veinlets
227 often show a common orientation and thus form bands of altered peridotites, surrounding
228 lenses of fresh granular peridotites (Fig. 3). Based on the field occurrences and lithological
229 associations, we selected a preserved area bearing primary associations from spinel- to

230 plagioclase-bearing lithotypes (black box in [Fig. 1](#)) to perform detailed mapping ([Fig. 3](#)) and
231 sampling.

232

233 **4. Sampling and Analytical Methods**

234 In the selected area ([Figs. 1, 3](#)), we collected samples along traverses showing
235 primary associations of spinel peridotite and spinel dunite, grading to plagioclase peridotite,
236 olivine-rich troctolite and troctolite. [Table 1](#) reports the modal composition of 22 samples,
237 namely 3 spinel peridotites, 3 spinel dunites, 6 plagioclase peridotites, 4 olivine-rich
238 troctolites (>75% modal olivine) and 6 troctolites (<75% modal olivine). We performed
239 structural EBSD mapping of all samples, and mineral major (EPMA) and trace element (LA-
240 ICP-MS) chemical analyses of 7 samples, namely 1 spinel peridotite, 1 spinel dunite, 1
241 plagioclase peridotite, 1 olivine-rich troctolite and 3 troctolites. Detailed methodologies for
242 EBSD, major and trace elements analyses can be found in [Supplementary Material](#).

243

244 **5. Petrography**

245 In granular spinel peridotites, olivine, orthopyroxene, clinopyroxene, and spinel are
246 coarse-grained, up to centimetre-size. Olivines and pyroxenes (orthopyroxene +
247 clinopyroxene) are deformed, and display kink bands and undulatory extinctions,
248 respectively. Clinopyroxenes and orthopyroxenes both show thin exsolution lamellae of the
249 complementary pyroxene. Spinel is mostly coarse-grained in the peridotite assemblage but it
250 is also found at the rim of mantle orthopyroxene porphyroclasts, as symplectitic intergrowths
251 of orthopyroxene + spinel \pm clinopyroxene, which have been related to cooling and
252 incorporation of the peridotites at lithospheric temperatures (970-1100°C) ([Rampone et al.,](#)
253 [2008](#)). Within the analyzed samples, spinel peridotites show a strong variation of modal
254 composition of olivine, from 58% to 78% by vol. ([Table 1](#)). Melt-rock reaction
255 microstructures, i.e. the development of undeformed olivine embayments replacing exsolved
256 orthopyroxene and clinopyroxene, are extensively observed in spinel peridotites with the
257 highest modal olivine contents (“reacted spinel peridotite” in this study), as previously
258 documented by [Rampone et al. \(2008\)](#) and [Piccardo and Guarnieri \(2010\)](#).

259 Spinel dunites associated to spinel peridotites are mostly characterized by a very
260 coarse-grained texture of olivines (up to 3 centimetres in size, [Fig.5a](#)), that display clear kink
261 bands and an irregular shape. In places, coarse-grained rounded spinels (up to millimetre-
262 size) form aligned trails within the dunite.

263 Spinel-bearing, plagioclase peridotites preserve locally the microstructural evidence
264 of the first reactive melt percolation: (1) deformation and exsolution in olivine and
265 pyroxenes, respectively; (2) olivine embayments partially replacing mantle pyroxenes and
266 [orthopyroxene + spinel] exsolutions. Further microstructures are indicative of melt
267 impregnation of the spinel-bearing peridotitic matrix. Interstitial plagioclase and
268 orthopyroxene crystallize at the expense of olivine and exsolved clinopyroxene. The most
269 impregnated peridotites are characterized by an enrichment up to 25% of modal interstitial
270 minerals (plagioclase + orthopyroxene ± clinopyroxene) (Table 1). In these samples, where
271 melt focuses to form gabbronoritic veinlets (Fig. 2c), the melt crystallizes both idiomorphic
272 orthopyroxene and clinopyroxene at the contact between the gabbronoritic veinlet and the
273 host peridotite, indicating that saturation of clinopyroxene is reached. These newly formed
274 magmatic minerals are free of exsolution and deformation, and can be recognized from the
275 mantle pyroxene relicts.

276 Within the replacive troctolitic bodies associated with plagioclase peridotites (Fig.
277 2d), the texture of the olivine matrix varies with the modal abundance of interstitial minerals.
278 Within olivine-rich troctolites (>75% modal olivine, Figs. 4a,b, 5b), olivines are coarse-
279 grained (up to centimetre-size), show irregular contacts and are often deformed with the
280 occurrence of kink bands (Fig. 5). Interstitial plagioclase is found at triple grain junctions
281 (Fig. 4a) and along olivine grain boundaries (Figs. 4b, 5c,d). Within the most impregnated
282 troctolites (<75% modal olivine, Figs. 4c,d, 5d), some olivines show smaller grain size
283 (millimetre-size) and are undeformed (Fig. 5d). However, troctolites still preserve coarse
284 deformed grains of olivine (Figs. 4d and 5d) in the most dunitic areas. The plagioclase occurs
285 as poikilitic crystals enclosing rounded small grains of olivine (Fig. 4d), and it is associated
286 in places to poikilitic clinopyroxene.

287

288 **6. Textural analysis**

289 Microstructural observations from spinel dunite to olivine-rich troctolite to troctolite
290 suggest a progressive variation of the texture of the olivine matrix with increasing modal
291 composition of interstitial phases. In order to quantify the textural evolution observed in these
292 samples, we used the EBSD maps, from which we obtain four textural parameters for each
293 sample: (1) the number of grains, (2) the grain area (μm^2), (3) the grain aspect ratio (long
294 axis/short axis of a grain), and (4) the grain shape factor (Perimeter / Equivalent Perimeter of
295 circle with the same area) (Mainprice et al., 2014; Methodology details in Supplementary

296 [Material](#)). The aspect ratio is indicative of the crystal elongation, and the shape factor is
297 indicative of the tortuosity of a the grain boundary. The textural parameters calculated for
298 each sample are reported in [Table 1](#), and are plotted in [Figure 6](#) against modal olivine
299 contents. At decreasing modal olivine (from 99% vol. in the spinel dunite to 70% vol. in the
300 troctolite) during the transition from spinel dunite to olivine-rich troctolite to troctolite, we
301 observe a global trend of increasing number of grains (from 12 to 59), coupled to decreasing
302 grain area (from 38mm² to 6mm²), aspect ratio (from 1.85 to 1.43) and shape factor (from
303 2.49 to 1.77) ([Fig. 6](#)). This is consistent with the observed microstructural evolution from
304 large irregular olivines in the spinel dunites to increasingly rounded small olivines in the most
305 impregnated troctolites ([Figs. 4 and 5](#)). Similar textural evolution was described by [Boudier](#)
306 ([1991](#)) in the Oman ophiolite mantle-crust transition zone, to explain the replacive formation
307 of wehrlites at the expense of dunites.

308

309 **7. Crystallographic Preferred Orientation of olivine**

310 The Mt.Maggiore peridotites, dunites, olivine-rich troctolites and troctolites are
311 characterized by a very coarse centimetric grain size, therefore the low number of grains does
312 not enable the quantification of the strength of Crystallographic Preferred Orientations (CPO)
313 by the J-index, defined as the volume-averaged integral of the squared orientation densities,
314 sensitive to peaks in the orientation distribution function (i.e. single grains when only a few
315 olivine crystals are analyzed; [Bunge, 1982](#); [Ben Ismail and Mainprice, 1998](#)). Olivine CPO
316 are thus used as qualitative indicators of first-order structural variations between the analyzed
317 lithologies. The interstitial minerals are mainly poikilitic and a single crystal can cover almost
318 the entire thin section, it is thus impossible to measure any CPO for plagioclase,
319 orthopyroxene and clinopyroxene crystallized from the impregnating melt. Representative
320 olivine CPO and 2-10° misorientation rotation axes for each described lithotype (spinel
321 peridotite, reacted spinel peridotite, spinel dunite, plagioclase peridotite, olivine-rich
322 troctolite, troctolite) are shown in [Figure 7](#).

323 Olivine in both unreacted spinel peridotite ([Fig. 7a](#)) and plagioclase peridotite ([Fig.](#)
324 [7d](#)) are characterized by an axial-[100] CPO, with [100] axis showing the strongest preferred
325 orientation in the foliation plane, [010] axis maximum oriented normal to the foliation plane,
326 and [001] maximum within the foliation plane. The dominant low-angle misorientations
327 within olivines are accommodated by both [001] and [010] rotation axes, with a maximum on
328 [001] ([Fig. 7](#)). This indicates that plastic deformation of olivine crystals was related to

329 dislocation creep with activation of (010)[100] slip system, the easiest at high temperatures
330 conditions (1100-1200°C), and (001)[100], another commonly observed slip system activated
331 at high temperature in olivine (Ben Ismail and Mainprice, 1998; Tommasi et al., 2000, Karato
332 et al., 2008; Drouin et al., 2010; Higgie & Tommasi, 2012). A joint activation of the two
333 described (010)[100] and (001)[100] slip systems in olivine is a common explanation to
334 account for the CPO in natural peridotites deformed under asthenospheric conditions
335 (Tommasi et al., 2000).

336 Olivines in the reacted spinel peridotite (Fig. 7b), spinel dunite (Fig. 7c), olivine-rich
337 troctolite (Fig. 7e) and troctolite (Fig. 7f) are characterized by an axial-[010] CPO, with the
338 strongest axis orientation being [010] normal to the foliation. Axial-[010] CPO have been
339 previously described in impregnated peridotites (Ben Ismail et al., 2001; Le Roux et al.,
340 2008; Tommasi et al., 2008), hybrid olivine-rich gabbroic rocks (Higgie and Tommasi, 2012,
341 2014), and experiments of melt segregation during deformation (Holtzman et al., 2003). The
342 development of such patterns has been explained by: (1) activation of dominant (010)[100],
343 together with (010)[001] slip systems (Tommasi et al., 2000; Mainprice et al., 2005); (2) 3D
344 deformation involving stretching in multiple directions in the foliation plane (Tommasi et al.,
345 1999); (3) static recrystallization (Tommasi et al., 2008); and (4) deformation in presence of
346 melt (Holtzman et al., 2003; Le Roux et al., 2008; Kaczmarek and Tommasi, 2011) (see
347 discussion below). The low-angle misorientations (2-10°) of olivine in these lithotypes are
348 mainly accommodated by [010] rotation axis (Fig. 7). From spinel dunite to olivine-rich
349 troctolite and troctolite, we observe a randomization of the orientation of the [100] axis.
350 Furthermore, from olivine-rich troctolite to troctolite, the misorientation along [010]
351 decreases in concentration, suggesting either an annealing with progressive impregnation or
352 the preferential corrosion of olivine grains along [010] subgrain boundaries (see discussion
353 below).

354

355 **8. Major and trace elements mineral compositions**

356 Major and trace elements compositions of minerals in the studied spinel peridotite,
357 plagioclase peridotite, spinel dunite, olivine-rich troctolite, and troctolites are reported in
358 Table S2-5 of Supplementary Material. The standard deviations of the mineral trace elements
359 analyses are reported in Table S6 of Supplementary Material. Overall, our data are consistent
360 with mineral compositions reported in previous studies on the Mt.Maggiore peridotitic body

361 (Rampone et al., 1997, 2008; Müntener and Piccardo, 2003; Piccardo and Guarnieri, 2010),
362 except for the trace element abundances of olivine, which constitute an entirely new data set.

363 Olivines from spinel peridotites, plagioclase peridotites, spinel dunites, olivine-rich
364 troctolites and troctolites show homogeneous major elements compositions at high Forsterite
365 ($Fo = 89.4-90.2$) and Ni (2514-3064 ppm) contents (Table S2). However, variations in trace
366 elements concentrations are observed between the described lithotypes. Olivines in spinel
367 peridotites show low contents of Ti (10-15 ppm), Y (0.01-0.02 ppm) and Zr (0.002-0.003
368 ppm), whereas higher contents in these elements (e.g. Ti = 41-94 ppm) at constant Fo values
369 are observed in olivines from dunite, olivine-rich troctolite and troctolite (Fig. 8). Similar
370 variations in trace elements (REE, Ti, Zr, Hf) at constant Fo content, ruling out a simple
371 fractional crystallization process, were documented in olivines of Erro-Tobbio olivine-rich
372 troctolites (Rampone et al., 2016), and interpreted as the result of melt-rock reaction
373 processes. Sanfilippo et al. (2014) reported enrichments in Ti/Y and Zr/Y in olivines of
374 Internal Ligurides and Pineto olivine-rich troctolites and troctolites, and they also ascribed
375 such variations to the reaction between the olivine matrix and a modified melt. Olivine REE
376 patterns show a significant variability between the analyzed lithotypes (Figs. 9a,b, 10a,b).
377 Olivines in spinel peridotites show low HREE abundances ($Yb_N = 0.05-0.095$ times C1), and
378 high HREE fractionation ($Dy_N/Yb_N = 0.05-0.08$), comparable to olivines from the Gakkel
379 Ridge lherzolites reported by D'Errico et al. (2016). Olivines in the plagioclase peridotite
380 show higher REE absolute concentrations ($Yb_N = 0.18-0.25$ times C1) at constant HREE
381 fractionation ($Dy_N/Yb_N = 0.05-0.07$). In the spinel dunite, olivines show higher REE
382 abundances relative to olivines in peridotites ($Yb_N = 0.3-0.38$ times C1). In terms of HREE,
383 they resemble olivines in olivine-rich troctolites from Mid-Atlantic Ridge (Drouin et al.,
384 2009) and Erro-Tobbio (Rampone et al., 2016), but they display lower MREE/HREE
385 fractionation ($Dy_N/Yb_N = 0.26-0.43$). Olivines from olivine-rich troctolite and troctolites have
386 similar REE composition. They also show enriched HREE absolute concentrations ($Yb_N =$
387 $0.26-0.59$), but at stronger HREE fractionation ($Dy_N/Yb_N = 0.10-0.19$).

388 Clinopyroxenes in the spinel peridotite, plagioclase peridotite and troctolite show
389 similar Mg-value interval ($Mg\# = 88.7-91.4$) to clinopyroxenes analyzed in the same
390 lithotypes by Rampone et al. (1997, 2008) (Table S3). Variations are observed in Ti and Al
391 concentrations between lithotypes, with low Ti ($TiO_2 = 0.20-0.29$ wt%) and high Al ($Al_2O_3 =$
392 $5.71-6.46$ wt%) concentrations in spinel peridotites, and higher Ti ($TiO_2 = 0.23-0.62$ wt%)
393 and lower Al ($Al_2O_3 = 3.39-6.02$ wt%) concentrations in plagioclase peridotite. As
394 documented by Rampone et al. (1997, 2008), clinopyroxene porphyroclasts in the plagioclase

395 peridotites show a high compositional variability from core to rim. Cores preserve the low-Ti,
396 high-Al signature, similar to the composition of clinopyroxenes porphyroclasts in spinel
397 peridotites, whereas the rims show higher Ti, and lower Al contents. A similar zoning is
398 observed in interstitial and poikilitic clinopyroxene from the troctolite, from relatively low-Ti
399 ($\text{TiO}_2 = 0.29\text{-}0.41$ wt%), and high-Al ($\text{Al}_2\text{O}_3 = 5.2\text{-}5.7$ wt%) cores to high-Ti ($\text{TiO}_2 = 0.44\text{-}$
400 0.91 wt%), and low-Al ($\text{Al}_2\text{O}_3 = 3.83\text{-}4.94$ wt%) rims. In both spinel and plagioclase
401 peridotites, clinopyroxenes show strong LREE depletion ($\text{Ce}_\text{N}/\text{Yb}_\text{N} = 0.018\text{-}0.044$), and flat
402 MREE-HREE patterns (Figs. 9c, 10c) comparable to clinopyroxene compositions reported in
403 depleted lherzolites from the Gakkel Ridge (D'Errico et al., 2016). Higher HREE absolute
404 compositions have been measured in clinopyroxene cores from plagioclase peridotites ($\text{Yb}_\text{N} =$
405 $7\text{-}12$ times C1). Clinopyroxenes in troctolites also exhibit significant LREE depletion
406 ($\text{Ce}_\text{N}/\text{Yb}_\text{N} = 0.015\text{-}0.043$). In all plagioclase-bearing lithotypes (peridotite and troctolite) the
407 rims of clinopyroxene show an enrichment in Ti, Sc, V, Y and MREE-HREE ($\text{Yb}_\text{N} = 12\text{-}15$
408 times C1), the development of convex-upward REE patterns and Eu negative anomalies, as
409 previously documented by Rampone et al. (2008) and Piccardo and Guarnieri (2010).

410 Plagioclase in the plagioclase peridotite, olivine-rich troctolite and troctolite show
411 high Anorthite contents ($\text{An} = 85.1\text{-}88.1$) and very low Sr abundances (15.5-24.6 ppm), as
412 previously documented by Rampone et al. (1997, 2008) and Piccardo and Guarnieri (2010)
413 (Table S4). In all studied samples, REE patterns of plagioclase are characterized by
414 significant and similar LREE depletion ($\text{Ce}_\text{N}/\text{Sm}_\text{N} = 0.19\text{-}0.49$). However, variations in
415 absolute REE concentrations are observed between the different lithotypes. The lowest
416 abundances are observed in plagioclase of plagioclase peridotites (e.g. $\text{Sm}_\text{N} = 0.2\text{-}0.4$ times
417 C1), whereas they progressively increase in troctolites ($\text{Sm}_\text{N} = 0.4\text{-}1.2$ times C1) and olivine-
418 rich troctolites ($\text{Sm}_\text{N} = 0.7\text{-}1.5$ times C1).

419 Orthopyroxene is only found in the spinel and plagioclase peridotites. It shows
420 homogeneous Mg-values ($\text{Mg}\# = 89.2\text{-}90.3$) in both lithotypes (Table S5). As observed for
421 clinopyroxene, the REE absolute concentrations of orthopyroxenes in the spinel peridotite
422 ($\text{Yb}_\text{N} = 1.9\text{-}2.5$ times C1, $\text{Ce}_\text{N}/\text{Yb}_\text{N} = 0.002\text{-}0.006$) are comparable to those of orthopyroxenes
423 in the Gakkel Ridge depleted lherzolites (D'Errico et al., 2016) (Figs. 9f, 10f). In the
424 plagioclase peridotite, orthopyroxenes show higher absolute REE concentrations ($\text{Yb}_\text{N} = 2.3\text{-}$
425 5 times C1) at similar REE fractionation ($\text{Ce}_\text{N}/\text{Yb}_\text{N} = 0.002\text{-}0.004$). They are consistent with
426 orthopyroxene compositions documented by the previous study of Rampone et al. (2008).

427

428 9. Discussion

429 **9.1 Origin of replacive dunites by spinel-facies reactive porous flow**

430 As reported in previous studies, the Mt. Maggiore peridotitic body records an olivine-
431 crystallizing, pyroxene-dissolving reactive melt percolation stage at spinel facies conditions
432 (Rampone et al., 1997, 2008; Müntener and Piccardo, 2003; Piccardo and Guarnieri, 2010).
433 This melt-rock interaction is documented by the development of olivine embayments
434 replacing mantle pyroxenes, and the partial dissolution of pyroxenite layers commonly
435 associated with the peridotites. The reacted lithotypes show a high modal variability, from
436 depleted spinel lherzolites to pyroxene-poor harzburgites until the formation of dunite bodies
437 in the most extensively reacted peridotites. The dunitic bodies are characterized by irregular
438 to straight contacts with the spinel peridotite (Fig. 2a) and show in places spinel trails that are
439 indicative of the former presence of a pyroxenite layer, completely dissolved during
440 extensive reactive porous flow (Fig. 2b). Despite the high modal variability during evolution
441 from spinel lherzolite to reacted harzburgite to spinel dunite, Rampone et al. (2008) reported
442 rather constant bulk-rock Mg-values ($Mg\# = 89.8-90.5$), and olivines accordingly define a
443 very narrow range of $Fo_{89.4-90.2}$ content variation. Constant bulk Mg-values at increasing
444 modal olivine follow reactive porous flow trends (Rampone et al., 2008) and are indicative of
445 a buffering of the percolating melt at $Mg\# \approx 75$ (i.e. in equilibrium with olivine Fo_{90} , Collier
446 and Kelemen, 2010) during reactive porous flow. All lines of evidence point to a replacive
447 origin of the dunites in the Mt. Maggiore peridotitic body. In the following, we discuss the
448 structural and geochemical variability of the olivine matrix accompanying the observed
449 evolution from spinel lherzolites to spinel harzburgites to spinel dunites.

450

451 *9.1.1 Structural evolution during dunitization*

452 The replacive formation of the dunitic bodies is driven by an olivine-crystallizing,
453 pyroxene-dissolving reactive porous flow in the spinel lherzolites. The modal olivine
454 enrichment from spinel lherzolites to reacted spinel peridotites to spinel dunites is observed
455 with the growth of the pre-existing olivines at the expense of ortho- and clinopyroxene,
456 through the development of olivine embayments corroding mantle pyroxenes. The growth of
457 olivine is confirmed by the observed olivine texture in the spinel dunites, namely very coarse
458 grains of olivine (up to 3cm in size, Fig. 6b), showing irregular shapes (Fig. 6d).

459 During the evolution from spinel lherzolite to reacted spinel peridotite to spinel dunite
460 (Fig. 7a,b,c), the olivine CPO progressively varies from an axial-[100] CPO in the spinel
461 lherzolite to an axial-[010] CPO in the spinel dunite. Axial-[100] olivine CPO is largely

462 described in natural peridotites (Tommasi et al., 2000; Soustelle et al., 2009, 2010) as the
463 result of dislocation creep and the joint activation of (010)[100] and (001)[100], the two
464 easiest slip systems in olivine at asthenospheric conditions (Tommasi et al., 2000).

465 The analyzed axial-[010] CPO in the spinel dunite is consistent with previously
466 reported olivine CPO in replacive dunites from French Polynesia xenoliths (Tommasi et al.,
467 2004). As already mentioned (see section “*Crystallographic Preferred Orientation of*
468 *olivine*”), the development of such patterns has been explained by several processes and
469 conditions (pressure, strain, water content; Karato et al., 2008; Jung et al., 2009). An axial-
470 [010] CPO of olivine can be formed by the joint activation of dominant (010)[100], together
471 with (010)[001] slip system (Tommasi et al., 2000; Mainprice et al., 2005), commonly
472 activated at high pressures (>3 GPa; Jung and Karato, 2001; Jung et al., 2009). However, the
473 Mt.Maggiore peridotites display microstructural evidence that the reactive melt percolation
474 forming replacive dunites occurred at spinel facies (Rampone et al., 2008; Piccardo and
475 Guarnieri, 2010), therefore, the pressure conditions are too low for activation of [001] glide
476 in olivine (Jung and Karato, 2001; Mainprice et al., 2005; Jung et al., 2009). Olivines in the
477 Mt.Maggiore dunites are deformed, irregular and very coarse-grained, thus the development
478 of axial-[010] CPO is not likely to be related to static recrystallization, as proposed by
479 Tommasi et al. (2008). Field and microstructural evidence support the formation of dunites
480 after extensive pyroxene-dissolving, olivine-crystallizing melt-rock interaction. Accordingly,
481 we infer that the CPO evolution observed in olivine from spinel lherzolite (axial-[100]) to
482 spinel dunite (axial-[010]) is due to deformation in presence of melt, as was described in
483 melt-bearing experiments of deformation (Holtzman et al., 2003) and in the Lherz refertilized
484 peridotites (Le Roux et al., 2008). Dunitic zones correspond to the most reacted lithotype,
485 thus to the strongest accumulation of melts over time. However, the preservation of a clear
486 olivine CPO implies that the instantaneous melt/rock ratio remained, during the whole
487 process of reactive porous flow, below the critical value allowing for loss of cohesion of the
488 solid matrix (20-40%; Rosenberg and Handy, 2005). The reacted spinel harzburgite (Fig. 7b)
489 is characterized by a transitional CPO of olivine, between the spinel lherzolite (Fig. 7a) and
490 the spinel dunite (Fig. 7c), with a decreasing concentration of the [100] axis and increasing
491 concentration of [010]. This is indicative of a progressive change of the CPO, as a function of
492 the cumulated melt fraction and strain (Higgie and Tommasi, 2012).

493 A change in the rotation axes accommodating the low-angle misorientations (<10°)
494 within olivine crystals is observed during the dunitization process. Olivines in spinel
495 lherzolites and spinel dunites show low-angle misorientation accommodated by both [001]

496 and [010] rotation axes, with major accommodation by [001] axis for olivines in spinel
497 lherzolites and major accommodation by [010] axis for olivines in spinel dunites. This
498 variation can be ascribed to a change in the preferential slip system activation of olivine, from
499 (010)[100] to (001)[100] in spinel peridotites and spinel dunites, respectively (Tommasi et
500 al., 2000).

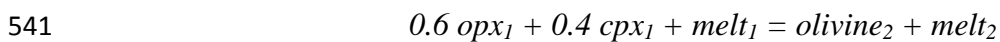
501

502 9.1.2 Chemical changes of percolating melt: REE modelling

503 No significant major and minor elements compositional variability is observed in
504 olivines from spinel peridotites and spinel dunites ($Fo = 89.4-90.2$, $Ni = 2500-3000\text{ppm}$). On
505 the other hand, olivines in the spinel dunites are characterized by much higher incompatible
506 trace elements contents (e.g. Ti, Zr, Y, Fig. 8) with respect to olivines in the spinel
507 peridotites. Also, they show higher absolute REE concentrations ($Yb_N = 0.3-0.38$ times $C1$)
508 coupled to lower MREE/HREE fractionation ($Dy_N/Yb_N = 0.26-0.43$) than olivines in spinel
509 peridotites ($Yb_N = 0.05-0.095$ times $C1$; $Dy_N/Yb_N = 0.05-0.08$) (Figs. 9a,b, 10a,b). In terms of
510 such trace elements, olivines in the spinel dunites more closely resemble olivines in the
511 troctolites, although bearing a different MREE/HREE fractionation (Fig. 9b).

512 To better understand the trace element variability related to the described process of
513 reactive melt percolation at spinel facies, we performed a geochemical modelling using Plate
514 Model numerical simulations (Vernières et al., 1997). This model reproduces a rock-
515 dominated reactive melt percolation, during which the composition of the melt is buffered by
516 the solid matrix, varying porosity and modal composition along the percolation column (Fig.
517 11). The selected host rock forming the mantle column is the depleted spinel lherzolite
518 MM2/12 from Rampone et al. (2008), whose modal composition (Ol:Opx:Cpx =
519 0.74:0.20:0.06) is similar to spinel peridotites analysed in this study (Table S7). The spinel
520 peridotites from Mt. Maggiore were previously interpreted as residual peridotites (Rampone et
521 al., 1997, 2008; Piccardo and Guarnieri, 2010) after 6% fractional melting, following the
522 equation of Johnson et al. (1990) and Warren (2016). Rampone et al. (1997, 2008), using
523 simple AFC modeling, inferred that melts percolating the spinel and plagioclase peridotites
524 (after the partial melting event) had also a LREE-depleted chemical signature. They
525 hypothesized that such depleted signature could either represent a primary characteristic of
526 the melt, or it was acquired during the reactive melt percolation through the depleted spinel
527 lherzolite (Rampone et al., 2008).

528 We performed the Plate Model numerical simulations (Vernières et al., 1997) with
529 different, variably LREE-depleted, initial melts. We noticed that an N-MORB starting
530 composition (Workman and Hart, 2005) although reproducing the MREE/HREE
531 fractionation and absolute concentrations of olivine in the spinel dunite, does not explain the
532 strong LREE-depletion of plagioclase and clinopyroxene analyzed in the plagioclase
533 peridotite and troctolite (Fig. S1). This observation, together with the evidence of preserved
534 LREE-depleted compositions of reacted spinel peridotites (Rampone et al., 2008),
535 corroborate the inference that the percolating melts had likely a primary LREE-depleted
536 signature. Accordingly, we selected an initial melt composition corresponding to a depleted
537 single melt increment obtained after 6% fractional melting of a slightly depleted mantle
538 source, consistent with previous assumptions (Rampone et al., 1997, 2008; Piccardo and
539 Guarnieri, 2010) (Fig. 11a, Table S7). In order to model the reactive percolation leading to
540 the replacive formation of the dunites, we assumed the following reaction:



542 in which mantle pyroxenes ($M_a = 60\% \text{ opx} + 40\% \text{ cpx}$) are dissolved by the incoming melt
543 (melt_1), while crystallizing olivine ($M_c = 100\% \text{ olivine}$), at global $[M_a/M_c] = 1.08$. The
544 partition coefficients used for olivine, orthopyroxene and clinopyroxene, after Warren (2016),
545 are reported in Table S7. The computed initial REE trace element compositions of
546 clinopyroxene and orthopyroxene in the host depleted lherzolite fit well the analyzed mineral
547 compositions (Fig. 11a), whereas discrepancies are observed between computed and analyzed
548 olivine REE compositions, both in terms of absolute concentrations and fractionation (Fig.
549 11a). We infer that the lower trace element abundances and stronger fractionation observed in
550 the analyzed olivine in spinel peridotite is the result of subsolidus reequilibration between
551 clinopyroxene and olivine, as described by Sun and Liang (2014). Calculated olivine–
552 clinopyroxene REE partitioning (Sun and Liang, 2012, 2013a,b, 2014) yield low equilibrium
553 temperature of 1000-1100°C (Fig. S2), consistent with the low equilibration temperature
554 (970-1100°C) calculated by different geothermometers (Ca in opx, Sc and V opx-cpx
555 partitioning; see Rampone et al, 2008) for the spinel facies equilibration in non-reacted
556 peridotites.

557 The reactive melt percolation in the spinel lherzolite column leads to the progressive
558 replacement of mantle pyroxenes by olivine, and thus to the formation of a dunite (Fig. 11).
559 During progressive reaction, the porosity in the rock column increases from 1% in the
560 starting lherzolite to 3% in the replacive dunite, as expected in a melt-rock reaction process
561 characterized by $[M_a/M_c] > 1$. The modified melt composition, i.e. the melt in equilibrium

562 with the spinel dunite (Fig. 11b, Table S7), shows global REE enrichment at constant LREE
563 fractionation, and olivine in equilibrium with the modified melt ($Yb_N = 0.35$ times C1,
564 $D_{Y_N}/Yb_N = 0.31$, Fig. 11b) fit well the analyzed HREE patterns of olivines in the spinel
565 dunite (Fig. 11b), both in terms of absolute concentration ($Yb_N = 0.3-0.38$ times C1) and
566 fractionation ($D_{Y_N}/Yb_N = 0.26-0.43$). We thus infer that the enriched REE compositions
567 measured in olivines from the spinel dunite are acquired by equilibration of the olivine matrix
568 with the percolating melt, modified after reactive porous flow in the spinel peridotites.

569 Olivines from the South Lanzo replacive dunites documented by Sanfilippo et al.
570 (2014, 2017) lower absolute trace element contents ($Yb_N = 0.21-0.31$ times C1; Ti = 26-33
571 ppm) than olivines in spinel dunites Mt.Maggiore (this study; $Yb_N = 0.3-0.38$ times C1).
572 However, Sanfilippo et al. (2014, 2017) interpreted these elongated replacive dunite bodies,
573 more than decametre-size, as dunite channels allowing focussed flow of a MORB-type melt.
574 They considered the lack of a “reactive signature” of incompatible trace elements in olivines
575 of Lanzo replacive dunites as reflecting equilibration with melts migrating through them by
576 channelized flow, at high melt/rock ratios (Kelemen et al., 1995b; Spiegelman and Kelemen,
577 2003). In the Mt.Maggiore peridotites, the studied dunites are found as metre-size dunitic
578 pods, and not as the elongated bodies commonly ascribed to channelized flow at high
579 melt/rock ratios (Kelemen et al., 1995a). We infer that dunite formation involved moderate
580 melt/rock ratios (consistent with the preservation of clear olivine CPOs described above),
581 which did not allow the formation of high-porosity dunite channels. The REE-enriched
582 patterns analyzed in olivines from the Mt.Maggiore spinel dunites (Fig. 11b) thus represent
583 the preserved “reactive signature” of incompatible elements, as a consequence of melt/rock
584 ratios involved in the reactive porous flow lower than those required to form high-porosity
585 dunite channels (Kelemen et al., 1995b; Sanfilippo et al., 2017).

586

587 **9.2 Origin of hybrid troctolites by plagioclase-facies melt impregnation**

588 At Mt.Maggiore, spinel peridotites (including clinopyroxene-poor spinel lherzolites,
589 reacted harzburgites and dunites) grade to plagioclase-bearing lithotypes across the
590 impregnation front observed at kilometre-scale in the field (Figs. 1, 3) (Rampone et al., 2008;
591 Piccardo and Guarnieri, 2010). The plagioclase peridotites show microstructures indicative of
592 an olivine-dissolving, [plagioclase + orthopyroxene]-crystallizing melt-rock interaction. In
593 the studied area, the plagioclase peridotites are in contact with metre-size troctolitic bodies
594 showing variable modal composition, from 70% to 90% of olivine (Fig. 5, Table 1) and up to

595 30% of interstitial minerals (plagioclase \pm clinopyroxene). These olivine-rich troctolites and
596 troctolites show similar microstructures to the plagioclase peridotites, indicative of an
597 olivine-dissolving, plagioclase-crystallizing melt-rock interaction. Olivine-rich troctolites and
598 troctolites also show large variations in trace element (Yb, Ti, Y, Zr) contents and HREE
599 fractionation of olivine (Figs. 8, 9, 10), at almost constant Fo = 89.4-90.2, difficult to
600 reconcile with a simple “cumulate” origin (Rampone et al., 1997; Piccardo and Guarnieri,
601 2010). Field, microstructural and geochemical evidence thus support a replacive origin of the
602 troctolitic bodies, likely related to the impregnation of pristine spinel dunites.

603 In the following, we discuss the textural and microstructural evolution of the olivine
604 matrix during impregnation of the spinel dunite and replacive formation of olivine-rich
605 troctolite and troctolite. We then discuss the depleted and SiO₂-rich chemical signature of
606 impregnating melts and provide a REE modelling of the melt impregnation process, to
607 account for the observed mineral compositions in the troctolites.

608

609 *9.2.1 Structural evolution during impregnation*

610 Textural variations related to dissolution-precipitation reactions and replacive
611 formation of olivine-rich troctolites have been extensively described in oceanic settings
612 (Drouin et al., 2010; Ferrando et al., this volume), ophiolites (Sanfilippo et al., 2013;
613 Rampone et al., 2016) and melt-rock interaction experimental studies (Van den Bleeken et
614 al., 2010; Saper and Liang, 2014; Francomme et al., this volume). The described hybrid
615 troctolites are characterized by rounded grains of olivines, enclosed in poikilitic minerals
616 crystallized from the percolating melt. Similar crystallographic orientations of neighbouring
617 rounded olivine grains suggest that they formerly belonged to a single olivine grain, corroded
618 and disrupted by the reactive melt (Suhr et al., 2008; Drouin et al., 2010). In this study, the
619 field-controlled geological setting enables the direct observation of the evolution of textures
620 from the dunitic protolith to the troctolitic end-product during progressive impregnation
621 process (i.e., at decreasing modal contents of olivine). Olivines in the dunite are deformed,
622 irregular and very coarse grained, up to 3 centimetres in size (Figs. 4, 5, 6). Olivine corrosion
623 in the dunite starts at triple grain junctions (Fig. 4a) and evolves following grain boundaries
624 (Fig. 4b), while crystallizing interstitial plagioclase. In the most impregnated samples, the
625 extensive corrosion of olivine leads to the disruption of large irregular olivines into several
626 smaller and rounded olivine grains (Fig. 4c,d) that are enclosed in the poikilitic plagioclase.
627 Disrupted olivines often show less deformation than the former dunitic olivine (Fig. 5),

628 suggesting a preferential corrosion along subgrain boundaries, as previously inferred by [Suhr](#)
629 [et al. \(2008\)](#) and [Drouin et al. \(2010\)](#) in the Mid-Atlantic Ridge olivine-rich troctolites.

630 The quantification of the textural evolution of the olivine matrix from spinel dunite to
631 troctolite reveals a correlation between the modal composition of olivine and the calculated
632 mean grain number, grain area, aspect ratio and shape factor ([Fig. 6](#)). During progressive
633 impregnation of the dunite (i.e. decreasing modal olivine), we observe an increase in grain
634 number (from 12 to 59), accompanied with a decrease in grain area (from 38mm² to 6mm²),
635 aspect ratio (from 1.85 to 1.43) and shape factor (from 2.49 to 1.77) of olivine grains ([Fig. 6](#)).
636 This evolution is indicative of the progressive corrosion and disruption of the dunitic matrix
637 by the reactive melt ([Fig. 5](#)) ([Drouin et al., 2010](#)). The end-product of the impregnation
638 process is a troctolite, composed of up to 30% of interstitial minerals, characterized by
639 undeformed small rounded olivine grains enclosed in poikilitic plagioclase and clinopyroxene
640 ([Figs. 4, 5, 6](#)). The decreasing concentration of the [010] olivine low-angle misorientation
641 from dunite to olivine-rich troctolite to troctolite ([Fig. 7c,e,f](#)) is consistent with the described
642 process of preferential corrosion along subgrain boundaries, and the decrease in grain
643 deformation during reaction and disruption of a coarse deformed olivine into several rounded
644 smaller olivines ([Suhr et al., 2008](#); [Drouin et al., 2010](#)). Our EBSD analyses demonstrate the
645 whole textural evolution, from the mantle protolith to the troctolite end-product, previously
646 inferred to explain the origin of olivine-rich troctolites in oceanic and ophiolitic settings
647 ([Suhr et al., 2008](#); [Drouin et al., 2010](#); [Sanfilippo et al., 2013](#); [Rampone et al., 2016](#)).
648 Magmatic cumulate textures in olivine-rich troctolites and troctolites can thus develop as a
649 consequence of dissolution-precipitation reactions in a mantle-derived protolith.

650 No major change of olivine CPO is observed during impregnation and replacive
651 formation of plagioclase peridotites and hybrid troctolites. Olivines in the plagioclase
652 peridotite show an axial-[100] CPO, and olivines in the troctolite show a axial-[010], similar
653 to the spinel lherzolite and spinel dunite protolith, respectively ([Fig. 7](#)). The preservation of
654 the protolith CPO of olivine in plagioclase peridotite and troctolite, suggests low
655 instantaneous melt-rock ratios involved in the impregnation process ([Higgie and Tommasi,](#)
656 [2012](#)). Our results differ from the olivine CPO randomization described during the replacive
657 formation of olivine-rich troctolites from the Atlantis Massif ([Drouin et al., 2010](#)), suggesting
658 melt/rock ratios allowing the loss of cohesion of the solid matrix. Overall, this indicates that
659 there is no universal CPO signature of melt-rock interactions originating hybrid troctolites
660 ([Drouin et al., 2010](#)), since the modification or preservation of the protolith CPO of olivine
661 entirely depends on the physical parameters (melt/rock ratio, temperature, pressure, strain,

662 water content; [Karato et al., 2008](#); [Jung et al., 2009](#)) involved in each melt-rock reaction
663 stage.

664

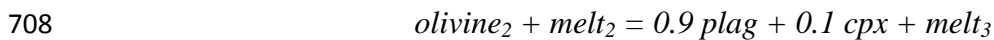
665 *9.2.2 Chemical signature of impregnating melts*

666 Despite being part of the same impregnation event crystallizing plagioclase +
667 orthopyroxene in the plagioclase peridotite, no interstitial orthopyroxene is found in the
668 troctolites. Numerous studies describe the impregnation of peridotites by a silica-saturated
669 melt, leading to the crystallization of plagioclase + orthopyroxene ([Dijkstra et al., 2003](#);
670 [Piccardo et al., 2007](#); [Rampone and Borghini, 2008](#); [Rampone et al., 2008](#); [Van den Bleeken,](#)
671 [2011](#); [Dygert et al., 2016](#)). They suggest that the impregnating melt acquired its silica-rich,
672 orthopyroxene-saturated signature during a previous pyroxene-dissolving, olivine-
673 crystallizing reactive porous flow in the spinel facies ([Rampone et al., 2008](#)). [Kelemen et al.](#)
674 [\(1995b\)](#) and [Dijkstra et al. \(2003\)](#) showed that melt fractions produced by shallow mantle
675 melting underneath mid-ocean ridges have more SiO₂-rich compositions than high-pressure
676 mantle melts, and are thus closer to orthopyroxene saturation ([Dijkstra et al., 2003](#)). The
677 reaction of these melts with the host harzburgitic wall-rock, dissolving pyroxenes and
678 crystallizing olivine, will rapidly drive the melt to orthopyroxene-saturation ([Kelemen et al.,](#)
679 [1995b](#); [Dijkstra et al., 2003](#)). The absence of interstitial orthopyroxene crystallization in the
680 troctolites suggests that the orthopyroxene saturation of impregnating melts observed in the
681 plagioclase peridotite is not only related to the spinel-facies reactive melt percolation, but
682 also to shallower dissolution-precipitation reactions involving pyroxene corrosion during
683 impregnation. Microstructures characterizing the impregnation stage indicate the corrosion of
684 olivine + mantle pyroxenes in the plagioclase peridotites ([Rampone et al., 2008](#); [Piccardo and](#)
685 [Guarnieri, 2010](#)), whereas only olivine is being corroded during impregnation of the spinel
686 dunite. Therefore, we infer that the difference in the melt-rock interaction occurring in
687 peridotites and dunites (peridotite-dissolution vs olivine-dissolution, respectively) lead to
688 local variations in the melt compositions, resulting in orthopyroxene saturation in the melt
689 percolating the peridotites ([Dijkstra et al., 2003](#)).

690 Previous studies of the Mt.Maggiore plagioclase peridotites and troctolites interpreted
691 the impregnating melts to be previously modified by the spinel facies reactive porous flow
692 ([Rampone et al., 1997, 2008](#)). They reported geochemical compositions of interstitial
693 minerals (clinopyroxene and plagioclase) in equilibrium with a LREE depleted, M-HREE-
694 enriched melt ([Rampone et al., 1997, 2008](#); [Piccardo and Guarnieri, 2010](#)). The M-HREE

695 enrichment was thought to be acquired during pyroxene-dissolving, olivine-crystallizing
696 reactive melt percolation (AFC modelling, Rampone et al., 2008). Our Plate Model numerical
697 simulation of the dunitization stage (see discussion above) confirms the M-HREE-enriched
698 signature of the melt modified after the spinel facies melt-rock interaction.

699 In order to explain the REE compositional variations documented in interstitial
700 minerals in the troctolite (Fig. 9c,e), as well as the observed change in HREE fractionation
701 between olivines in the dunite ($Dy_N/Yb_N = 0.26-0.43$) and in the troctolite ($Dy_N/Yb_N = 0.10-$
702 0.19) (Fig. 9b), we performed a second step of Plate Model simulation of the impregnation
703 process in the spinel dunites (Fig. 12a). The selected host rock and input melt composition
704 are the output of the first stage of reactive melt percolation, namely a spinel dunite (100%
705 olivine, 3% porosity, $Yb_N = 0.35$ times C1, $Dy_N/Yb_N = 0.31$) impregnated by a LREE-
706 depleted, M-HREE-enriched melt, modified during the spinel-facies reactive percolation
707 (Table S7). We assumed the following reaction:



709 in which olivine ($M_a = 100\%$ olivine) is dissolved by the impregnating melt ($melt_2$), while
710 crystallizing interstitial plagioclase and clinopyroxene ($M_c = 90\%$ plagio + 10% cpx), at
711 global [$M_a/M_c = 0.96$]. Partition coefficients used for olivine and clinopyroxene were the
712 same as those used for the spinel facies reactive percolation stage (Table S7). For plagioclase,
713 we used a selected compilation of partition coefficients from Bedard (2001); Aigner-Torres et
714 al. (2007) and Laubier et al. (2014) (Table S7).

715 Plate Model results show that the impregnation of the spinel dunite progressively
716 leads to the dissolution of olivine and to the crystallization of plagioclase and clinopyroxene,
717 thus causing the replacive formation of a hybrid troctolite composed of Ol:Plag:Cpx =
718 $0.73:0.25:0.02$ (Fig. 12b), similar to what is observed in the field (Table 1). The porosity
719 decreases during impregnation, from 3% in the spinel dunite to 2% in the troctolite, as
720 expected from a process characterized by a [M_a/M_c] < 1. The modified melt composition, i.e.
721 in equilibrium with the replacive troctolite, preserves its LREE depletion and is slightly less
722 enriched in M-HREE (up to 28 times C1, Table S7) with respect to the input melt (Fig. 12b).
723 A remarkable feature is the development of a negative Eu anomaly in the modified melt
724 composition after crystallization of plagioclase.

725 Plagioclase in equilibrium with the modified melt fit well the analyzed compositions
726 of plagioclase cores in the troctolites, both in terms of LREE fractionation and absolute REE
727 concentrations (Fig. 12b). It is remarkable, however, that plagioclase REE contents display
728 large variations at constant LREE fractionation both between different lithotypes and within

729 single grains (e.g. cores of large crystals vs. thin interstitial rims). Specifically, the
730 progressive decrease in interstitial plagioclase modal content from troctolite to olivine-rich
731 troctolite is correlated with an enrichment in plagioclase trace elements absolute
732 concentrations (Sm_N up to 1.5 times C1) (Figs. 9, 10). As for plagioclase, computed
733 clinopyroxene in equilibrium with the modified melt fit well the analyzed compositions of
734 clinopyroxene cores in the troctolite. However, we observed significant REE enrichments at
735 the rims of large clinopyroxene crystals, as well as in thin interstitial grains (Figs. 9, 10),
736 similar to what was described in previous papers (Rampone et al., 1997, 2008; Piccardo and
737 Guarnieri, 2010). In these studies, within-grain variations in interstitial minerals (plagioclase
738 and clinopyroxene) were interpreted as the effect of late-stage crystallization of trapped melt
739 fractions.

740 Computed olivine in equilibrium with the troctolite-forming melt shows lower HREE
741 absolute concentrations and MREE/HREE fractionation ($Yb_N = 0.29$ times C1, $Dy_N/Yb_N =$
742 0.3) than olivines analyzed in the troctolite ($Yb_N = 0.26-0.59$ times C1, $Dy_N/Yb_N = 0.10-0.19$)
743 (Fig. 12b). This discrepancy cannot be explained by a subsolidus reequilibration between
744 clinopyroxene and olivine (Sun and Liang, 2014), since most of the troctolites are composed
745 exclusively of olivine + interstitial plagioclase (Fig. 5; Table 1). Moreover, subsolidus
746 reequilibration with clinopyroxene would lower HREE absolute contents of olivine (Sun and
747 Liang, 2014), as observed in spinel peridotite (see discussion above), whereas HREE contents
748 of olivine in the troctolites are higher than the computed olivine in equilibrium with the
749 impregnating melt (Fig. 12b). This is further supported by high equilibration temperatures
750 (1150°C and 1250°C) computed using olivine-clinopyroxene HREE partitioning in troctolite
751 (Sun and Liang, 2012, 2013a,b, 2014) (Fig. S2), consistent with previous geothermometric
752 estimates of the impregnation stage reported by Rampone et al. (2008).

753 In order to explain the REE enrichments in interstitial plagioclase and clinopyroxene
754 as well as the stronger MREE/HREE fractionation in olivine of troctolites, we have modelled
755 further crystallization steps at decreasing melt mass, resulting in the closure of the porosity
756 (Fig. 13). The $[M_a/M_c]$ ratio varies along the reaction process from 0.72 to 0.27 for the final
757 crystallization step. During the progressive crystallization and decrease in porosity (from 2%
758 to 0.47%), the melt composition evolves towards a fractionated HREE-enriched composition.
759 Olivines in equilibrium with this HREE-enriched melt ($Yb_N = 0.54$ times C1; $Dy_N/Yb_N = 0.2$)
760 fit the analyzed MREE-HREE concentrations of olivine in the troctolites ($Yb_N = 0.26-0.59$
761 times C1, $Dy_N/Yb_N = 0.10-0.19$) (Fig. 13a). Lower MREE absolute concentrations analysed
762 in some olivine grains (see the grey field in Figure 13a) could reflect subsolidus

763 reequilibration between clinopyroxene and olivine (Sun and Liang, 2012, 2013a,b, 2014)
764 (Fig. S2), decreasing olivine absolute REE concentrations and Dy_N/Yb_N fractionation (Sun
765 and Liang, 2014).

766 During the last increments of crystallization (from 0.47% to 0.13% porosity), the melt
767 shows a global REE enrichment, while preserving its LREE fractionation (Fig. 13b,c).
768 Plagioclase and clinopyroxene in equilibrium with the progressively REE-enriching melt
769 cover the range of variation analyzed in crystal cores and rims of the plagioclase peridotite,
770 olivine-rich troctolite and troctolite, both in terms of absolute REE concentrations and LREE
771 fractionation (Fig. 13b,c). The modelled process of impregnation at decreasing melt mass
772 (from 2% to 0.13% porosity) is consistent with the process of trapped melt crystallization
773 previously proposed by Rampone et al. (1997, 2008) and Piccardo and Guarnieri (2010) to
774 explain the trace elements (Ti, Zr, Y, REE) enrichments analyzed at the rims of large
775 clinopyroxene crystals (Figs. 9, 10). The correlation between the plagioclase absolute REE
776 concentrations and modal content of olivine (REE enrichments at higher modal content of
777 olivine) is indicative of an increased contribution of trapped melt crystallization in olivine-
778 rich zones, and thus of lower instantaneous melt/rock ratios during their impregnation.

779

780 **Summary and concluding remarks**

781 The Mt.Maggiore peridotitic body is an ideal case study to investigate the field-
782 controlled evolution from spinel lherzolite to spinel dunite to hybrid troctolite (Fig. 14), after
783 two distinct melt-rock interaction processes. The first melt-rock interaction is an olivine-
784 crystallizing pyroxene-dissolving reactive percolation of a LREE-depleted melt, ultimately
785 resulting in the formation of replacive dunite at spinel facies. This stage led to: (1) olivine
786 growth at the expense of mantle pyroxenes, and development of very coarse and irregular
787 texture of the olivine matrix in the spinel dunite, (2) structural changes of olivine CPO from
788 axial-[100] in the spinel lherzolite to axial-[010] in the replacive dunite, (3) REE enrichment
789 in the olivine matrix during progressive dunitization.

790 At shallower plagioclase facies, the melt impregnation of the spinel lherzolites and
791 dunites caused the replacive formation of plagioclase peridotites and hybrid troctolites,
792 respectively. This olivine-dissolving, [plagioclase + clinopyroxene]-crystallizing melt-rock
793 interaction is documented in the troctolites by: (1) partial dissolution and disruption of the
794 dunitic olivine matrix by low instantaneous melt/rock ratios, leading to a textural evolution
795 towards small rounded undeformed olivine grains enclosed in poikilitic plagioclase, (2)

796 preservation of the olivine CPO from the spinel-facies protoliths, (3) crystallization of LREE-
797 depleted, HREE-enriched interstitial clinopyroxene and plagioclase from the melt modified
798 after reactive melt percolation, and change of the MREE-HREE fractionation in the olivine
799 matrix, and (4) REE enrichments in clinopyroxene rims and interstitial plagioclase during
800 late-stage trapped melt crystallization.

801 The field-controlled study of the evolution from spinel lherzolite protolith to the
802 troctolite end-product points to the possible CPO and geochemical inheritance from the
803 protolith during processes of melt-rock interaction (depending on the involved melt-rock
804 ratio). As a result, the structural and geochemical features analyzed in hybrid lithotypes are
805 representative not only of the last event of melt-rock interaction, but of the whole evolution
806 from mantle protolith to hybrid end-product. Olivine is the only mineral present in all
807 lithotypes during the evolution from mantle lherzolites to replacive dunites to hybrid
808 troctolites, therefore trace elements analyses in olivine are a perfect tool to investigate these
809 melt-rock interaction processes and a good understanding of trace elements behaviour in
810 olivine is of utmost importance.

811

812 **Acknowledgements**

813 We would like to thank Paolo Campanella and Alessandra Gavoglio, as well as
814 Christophe Nevado and Doriane Delmas for the realisation of the thin section and the high-
815 quality polishing. We also thank Fabrice Barou for assistance with the EBSD analyses,
816 Andrea Risplendente for assistance with the EPMA analyses, and Vincent Faucheux for
817 assistance with field work. This project has been supported by the People Programme (Marie
818 Curie Actions) of the European Union's Seventh Framework Programme FP7/2007–2013/
819 under REA-Grant Agreement No. 608001, 'ABYSS'.

820 **FIGURE CAPTIONS**

821

822 **Figure 1:** Geological map of the lithological variations and associated structures of the Mt.Maggiore
823 peridotites (Corsica). This structural map merges new data measured on the field with the data of
824 [Jackson and Ohnenstetter \(1981\)](#). The black square represents the area studied into more detail, where
825 the sampling has been done (see [Fig. 3](#) for more detail).

826

827 **Figure 2:** Representative lithological associations of the Monte Maggiore peridotitic body. A:
828 Plagioclase peridotite grading to plagioclase-poor dunite; B: Spinel dunite showing spinel-rich zones;
829 C: Strongly impregnated plagioclase peridotite, where the percolating melt segregated into
830 gabbronoritic veinlets; D: Plagioclase peridotite grading to ol-rich troctolite; E: Troctolite.

831

832 **Figure 3:** A: Representative sketch of the measured structures and lithological associations of the
833 Mt.Maggiore peridotites in the sampling area; B: Structural cross-section along the A-A' line
834 (indicated in the representative sketch); C: Three-dimensional lithological variations of the preserved
835 spinel- and plagioclase-peridotite lenses and associated mantle structures.

836

837 **Figure 4:** Microstructural evolution with increasing impregnation of a spinel dunite. A: Ol-rich
838 troctolite, plagioclase crystallized at the triple grain junction, and partly corroded pre-existing olivine;
839 B: Ol-rich troctolite, plagioclase corroded olivine along grain boundaries; C: Troctolite, interstitial to
840 poikilitic plagioclase surrounds smaller olivine grains; D: Troctolite, poikilitic plagioclase includes
841 rounded olivines. In the top left corner, an olivine is almost completely disrupted into two different
842 rounded grains. The dashed red lines highlight a kink band in a coarse deformed olivine.

843

844 **Figure 5:** EBSD phase (left column) and misorientation (right column) maps showing the textural
845 evolution of the olivine matrix with ongoing impregnation (decreasing modal olivine from A to D). A:
846 Spinel dunite M15-14, 99% olivine; B: Ol-rich troctolite M15-9, 85% olivine; C: Troctolite M15-8A,
847 73% olivine; D: Troctolite M15-8B, 73% olivine. The 0-10° scale indicates misorientation from the
848 average orientation of a grain.

849

850 **Figure 6:** Evolution of textural parameters of olivine plotted against the modal composition of olivine
851 in samples from spinel dunite to ol-rich troctolite and troctolite. A: Number of grains; B: Grain area;
852 C: Aspect Ratio; D: Shape Factor.

853

854 **Figure 7:** Representative olivine Crystallographic Preferred Orientation and 2-10 degrees
855 misorientation Inverse Pole Figures of the described lithotypes from Mt.Maggiore peridotitic body. A:

856 Spinel lherzolite M15/7B; B: Reacted spinel harzburgite M15/13; C: Spinel dunite M15/05; D:
857 Plagioclase peridotite M15/12B; E: Olivine-rich troctolite M15/1; F: Troctolite M15/8A.

858

859 **Figure 8:** Forsterite (mol%) vs selected trace elements in olivine. A: Yb normalized to C1-chondrite,
860 normalizing values after [Sun and McDonough \(1989\)](#); B: Ti (ppm); C: Y (ppm); D: Zr (ppm).
861 Compositional fields after [Rampone et al. \(2016\)](#); (1) Peridotites, (2) Troctolites, (3) Olivine gabbros;
862 and single analyses from [Sanfilippo et al. \(2014\)](#).

863

864 **Figure 9:** C1-normalized REE composition of rock-forming minerals. A: Olivine in spinel and
865 plagioclase peridotite; B: Olivine in spinel dunite, ol-rich troctolite and troctolite; C: Clinopyroxene in
866 spinel and plagioclase peridotite; D: Clinopyroxene in troctolite; E: Plagioclase; F: Orthopyroxene.
867 C1-chondrite normalization values after [Sun and McDonough \(1989\)](#). The compositional fields
868 represent Gakkel Ridge abyssal lherzolites from [D'Errico et al. \(2016\)](#), Mid-Atlantic Ridge olivine-
869 rich troctolites from [Drouin et al. \(2009\)](#), Erro Tobbio ophiolitic troctolites from [Rampone et al.](#)
870 [\(2016\)](#), and Mt.Maggiore plagioclase peridotites and troctolites from [Rampone et al. \(1997, 2008\)](#).
871 The solid red line is the average of the residual lherzolite field after [Warren \(2016\)](#). For
872 clinopyroxene, a distinction is made between cores (full symbol) and rims (empty symbols) of
873 crystals.

874

875 **Figure 10:** Primitive Mantle-normalized trace elements compositions of the rock-forming minerals.
876 A: Olivine in spinel and plagioclase peridotite; B: Olivine in spinel dunite, ol-rich troctolite and
877 troctolite; C: Clinopyroxene in spinel and plagioclase peridotite; D: Clinopyroxene in troctolite; E:
878 Plagioclase; F: Orthopyroxene. Primitive Mantle normalization values are after [Sun and McDonough](#)
879 [\(1989\)](#). The compositional fields are similar to Fig. 9. For Clinopyroxene, a distinction is made
880 between cores (full symbol) and rims (empty symbols) of crystals.

881

882 **Figure 11:** Evolution of chondrite-normalized REE abundances and modal compositions computed by
883 numerical simulation (Plate model, [Vernières et al., 1997](#)) during a process of reactive melt
884 percolation at spinel facies. Detail of input parameters is given in the text. C1-chondrite normalization
885 values are after [Sun and McDonough \(1989\)](#). A: initial stage, spinel lherzolite; B: dunite formed after
886 reactive melt percolation.

887

888 **Figure 12:** Evolution of chondrite-normalized REE abundances and modal compositions computed by
889 numerical simulation (Plate model, [Vernières et al., 1997](#)) during a process of impregnation at
890 plagioclase facies. Detail of input parameters is given in the text. C1-chondrite normalization values
891 after [Sun and McDonough \(1989\)](#). A: initial stage, spinel dunite; B: troctolite formed after melt
892 impregnation.

893

894 **Figure 13:** Evolution of chondrite-normalized REE abundances of rock-forming minerals by
895 numerical simulation (Plate Model, Vernières et al., 1997) during last steps of impregnation at
896 decreasing melt mass and closure of porosity. Detail of input parameters is given in the text. C1-
897 chondrite normalization values after Sun and McDonough (1989). A: olivine; B: Clinopyroxene; C:
898 Plagioclase.

899

900 **Figure 14:** Representative sketch of the textural evolution from spinel lherzolite to troctolite during
901 multi-stage melt-rock interaction history.

902

903 REFERENCES

904

905 Aigner-Torres, M., Blundy, J., Ulmer, P. and Pettke, T., 2007. Laser Ablation ICPMS study
906 of trace element partitioning between plagioclase and basaltic melts: an experimental approach.
907 Contributions to Mineralogy and Petrology, 153, 647-667, doi: 10.1007/s00410-006-0168-2.

908

909 Bédard, J.H., 2001. Parental magmas of the Nain Plutonic Suite anorthosites and mafic
910 cumulates: a trace element modelling approach. Contributions to Mineralogy and Petrology, 141, 747-
911 771, doi: 10.1007/s004100100268.

912

913 Ben Ismail, W., Mainprice, D., 1998. An olivine fabric database: an overview of upper mantle
914 fabrics and seismic anisotropy. Tectonophysics, 296, 145-157, doi: 10.1016/S0040-1951(98)00141-3.

915

916 Ben Ismail, W., Barruol, G. and Mainprice, D., 2001. The Kaapvaal craton seismic
917 anisotropy: petrophysical analyses of upper mantle kimberlite nodules. Geophysical Research Letters,
918 28, 2497-2500, doi: 10.1029/2000GL012419.

919

920 Borghini, G., Rampone, E., Crispini, L., De Ferrari, R. and Godard, M., 2007. Origin and
921 emplacement of ultramafic-mafic intrusions in the Erro-Tobbio mantle peridotite (Ligurian Alps,
922 Italy), Lithos, 94, 210-229, doi: 10.1016/j.lithos.2006.06.014.

923

924 Boudier, F., 1991. Olivine xenocrysts in picritic magmas: an experimental and microstructural
925 study. Contributions to Mineralogy and Petrology, 109, 114-123.

926

927 Bunge, H. J., 1982. Texture analysis in material sciences. Butterworths, London

928

929 Collier, M.L., Kelemen, P.B., 2010. The case for reactive crystallization at Mid-Ocean
930 Ridges. Journal of Petrology, 51, 1913-1940, doi: 10.1093/petrology/egq043.

931

932 Coumans, J.P., Stix, J., Clague, D.A., Minarik, W.G. and Layne, G.D., 2016. Melt-rock
933 interaction near the Moho: Evidence from crystal cargo in lavas from near-ridge seamounts,
934 Geochimica et Cosmochimica Acta, 191, 139-164, doi: 10.1016/j.gca.2016.07.017.

935

936 D'Errico, M.E., Warren, J.M. and Godard, M., 2016. Evidence for chemically heterogeneous
937 Arctic mantle beneath the Gakkel Ridge. *Geochimica et Cosmochimica Acta*, 174, 291-312, doi:
938 10.1016/j.gca.2015.11.017.
939

940 De Hoog, J.C.M., Gall, L. and Cornell, D.H., 2010. Trace-element geochemistry of mantle
941 olivine and application to mantle petrogenesis and geothermobarometry. *Chemical Geology*, 270,
942 196-215, doi: 10.1016/j.chemgeo.2009.11.017.
943

944 Dick, H.J.B., Tivey, M.A. and Tucholke, B.E., 2008. Plutonic foundation of a slow-spreading
945 ridge segment: Oceanic core complex at Kane Megamullion, 23°30'N, 45°20'W. *Geochemistry,*
946 *Geophysics, Geosystems*, 9, Q05014, doi: 10.1029/2007GC001645.
947

948 Dick, H.J.B., Lissenberg, C.J. and Warren, J.M., 2010. Mantle melting, melt transport, and
949 delivery beneath a Slow-Spreading Ridge: The Paleo-MAR from 23°15'N to 23°45'N. *Journal of*
950 *Petrology* 51, 425–467, doi: 10.1093/petrology/egp088.
951

952 Dijkstra, A.H., Drury, M.R. and Vissers, R.L.M., 2001. Structural petrology of plagioclase
953 peridotites in the West Othris Mountains (Greece): Melt impregnation in mantle lithosphere. *Journal*
954 *of Petrology*, 42, 5-24, doi: 10.1093/petrology/42.1.5.
955

956 Dijkstra, A.H., Barth, M.G., Drury, M.R., Mason, P.R.D. and Vissers, R.L.M., 2003. Diffuse
957 porous melt flow and melt-rock reaction in the mantle lithosphere at a slow-spreading ridge: A
958 structural petrology and LA-ICP-MS study of the Othris Peridotite Massif (Greece). *Geochemistry,*
959 *Geophysics, Geosystems*, 4, 8613, doi: 10.1029/2001GC000278.
960

961 Drouin, M., Godard, M., Ildefonse, B., Bruguier, O. and Garrido, C.J., 2009. Geochemical
962 and petrographic evidence for magmatic impregnation in the oceanic lithosphere at Atlantis Massif,
963 Mid-Atlantic Ridge (IODP Hole U1309D, 30°N). *Chemical Geology*, 264, 71-88, doi:
964 10.1016/j.chemgeo.2009.02.013.
965

966 Drouin, M., B. Ildefonse, and M. Godard, 2010. A microstructural imprint of melt
967 impregnation in slow spreading lithosphere: Olivine-rich troctolites from the Atlantis Massif,
968 Mid-Atlantic Ridge, 30°N, IODP Hole U1309D, *Geochemistry, Geophysics and Geosystems*, 11,
969 Q06003, doi:10.1029/2009GC002995.
970

971 Dygert, N., Liang, Y. and Kelemen, P.B., 2016. Formation of plagioclase lherzolite and
972 associated Dunite-Harzburgite-Lherzolite sequences by multiple episodes of melt percolation and
973 melt-rock reaction: an example from the Trinity ophiolite, California, USA. *Journal of Petrology*, 57,
974 815-838, doi: 10.1093/petrology/egw018.
975

976 Ferrando, C., Godard, M., Ildefonse, B. and Rampone, E., this issue. Melt transport and
977 mantle assimilation at Atlantis Massif (IODP Site U1309): evidence from chemical profiles along
978 olivine crystallographic axes. *Lithos*, this volume.
979

980 Foley, S.F., Prelevic, D., Rehfeldt, T. and Jacob, D.E., 2013. Minor and trace elements in
981 olivines as probes into early igneous and mantle melting processes. *Earth and Planetary Science*
982 *Letters*, 363, 181-191, doi: 10.1016/j.epsl.2012.11.025.
983

984 Francomme, J.E., Fumagalli, J., Borghini, G. and Capitani, G.C., this issue. Role of pressure
985 and melt composition on olivine-rich troctolite formation through reactive dissolution and
986 crystallization: an experimental study at 0.5 and 0.7 GPa. *Lithos*, this volume
987

988 Günther, D. and Heinrich, C., 1999. Enhanced sensitivity in laser ablation-ICP mass
989 spectrometry using helium-argon mixtures as aerosol carrier. *Journal of Analytical Atomic*
990 *Spectrometry*, 14, 1363–1368, doi: 10.1039/A901648A.
991

992 Hielscher, R., and Schaeben, H., 2008. A novel pole figure inversion method: specification of
993 the MTEX algorithm. *Journal of Applied Crystallography*, 41, 1024-1037, doi:
994 10.1107/S0021889808030112.
995

996 Higgie, K. and Tommasi, A., 2012. Feedbacks between deformation and melt distribution in
997 the crust-mantle transition zone of the Oman ophiolite. *Earth and Planetary Science Letters*, 359-360,
998 61-72, doi: 10.1016/j.epsl.2012.10.003.
999

1000 Higgie, K. and Tommasi, A., 2014. Deformation in a partially molten mantle: Constraints
1001 from plagioclase lherzolites from Lanzo, western Alps. *Tectonophysics*, 615-616, 167-181, doi:
1002 10.1016/j.tecto.2014.01.007.
1003

1004 Holtzman, B.K., Kohlstedt, D.L., Zimmerman, M.E., Heidelbach, F., Hiraga, T. and Hustoft,
1005 J., 2003. Melt segregation and strain partitioning: Implications for seismic anisotropy and mantle
1006 flow. *Science*, 301, 1227-1230, doi: 10.1126/science.1087132.
1007

1008 Jackson, M.D., Ohnenstetter, M., 1981. Peridotite and Gabbroic structures in the Monte
1009 Maggiore Massif, Alpine Corsica. *Journal of Geology*, 89, 703-719, doi: 0022-1376/81/8906-003.
1010

1011 Jochum, K. P., Nohl, U., Herwig, K., Lammel, E., Stoll, B. and Hofmann, A. W., 2005.
1012 GeoReM: A New Geochemical Database for Reference Materials and Isotopic Standards.
1013 *Geostandards and Geoanalytical Research*, 29, 333–338. doi: 10.1111/j.1751-908X.2005.tb00904.x.
1014

1015 Johnson, K.T.M., Dick, H.J.B. and Shimizu, N., 1990. Melting in the oceanic upper mantle:
1016 An Ion Microprobe study of diopsides in abyssal peridotites. *Journal of Geophysical research*, 95,
1017 2661-2678, doi: 10.1029/JB095iB03p02661.
1018

1019 Jung, H., Karato, S., 2001. Water-induced fabric transitions in olivine. *Science*, 293, 1460-
1020 1463, doi: 10.1126/science.1062235.
1021

1022 Jung, H., Mo, W. and Green, H.W., 2009. Upper mantle seismic anisotropy resulting from
1023 pressure-induced slip transition in olivine. *Nature Geoscience*, 2, 73-77, doi: 10.1038/NGEO389.
1024

1025 Kaczmarek, M.A., Tommasi, A., 2011. Anatomy of an extensional shear zone in the mantle,
1026 Lanzo massif, Italy. *Geochemistry, Geophysics, Geosystems*, 12, Q0AG06, doi:
1027 10.1029/2011GC003627.
1028

1029 Karato, S., Jung, H., Katayama, I. and Skemer, P., 2008. Geodynamic significance of seismic
1030 anisotropy of the Upper Mantle: new insights from laboratory studies. *Annual Review Earth Planetary*
1031 *Science*, 36, 59-95, doi: 0084-6597/08/0530-0059.

1032
1033 Kelemen, P.B., Shimizu, N. and Salters, V.J.M., 1995a. Extraction of mid-ocean-ridge basalt
1034 from the upwelling mantle by focused flow of melt in dunite channels. *Nature*, 375, 747-753, doi:
1035 10.1038/375747a0.
1036
1037 Kelemen, P.B., Whitehead, J.A., Aharonov, E. and Jordahl, K.A., 1995b. Experiments on
1038 flow focusing in soluble porous media, with applications to melt extraction from the mantle. *Journal*
1039 *of Geophysical Research*, 100, 475-496, doi: 10.1029/94JB02544.
1040
1041 Kelemen, P.B., Braun, M. and Hirth, G., 2000. Spatial distribution of melt conduits in the
1042 mantle beneath oceanic spreading ridges: Observations from the Ingalls and Oman ophiolites.
1043 *Geochemistry, Geophysics, Geosystems*, 1, doi: 10.1029/1999GC000012.
1044
1045 Kelemen, P.B., Kikawa, E., Miller, D.J. and Shipboard Scientific Party, 2007. 1. Leg 209
1046 Summary: Processes in a 20-km-thick conductive boundary layer beneath the Mid-Atlantic Ridge,
1047 14°-16°N. *Proceedings of the Ocean Drilling Program, Scientific Results Volume 209: College*
1048 *Station TX (Ocean Drilling Program)*, 1-33, doi: 10.2973/odp.proc.sr.209.001.2007.
1049
1050 Lambart, S., Laporte, D. and Schiano, P., 2009. An experimental study of focused magma
1051 transport and basalt-peridotite interactions beneath mid-ocean ridges: implications for the generation
1052 of primitive MORB compositions. *Contributions to Mineralogy and Petrology*, 157, 429-451, doi:
1053 10.1007/s00410-008-0344-7.
1054
1055 Laubier, M., Grove, T.L. and Langmuir, C.H., 2014. Trace element mineral/melt partitioning
1056 for basaltic and basaltic andesitic melts: An experimental and laser ICP-MS study with application
1057 to the oxidation state of mantle source regions. *Earth and Planetary Science Letters*, 392, 265-278, doi:
1058 10.1016/j.epsl.2014.01.053.
1059
1060 Laukert, G., Von der Handt, A., Hellebrand, E., Snow, J.E., Hoppe, P. and Klügel, A., 2014.
1061 High-pressure reactive stagnation recorded in abyssal pyroxenites from the ultraslow-spreading Lena
1062 Trough, Arctic Ocean. *Journal of Petrology*, 55, 427-458, doi: 10.1093/petrology/egt073.
1063
1064 Le Roux, V., Tommasi, A. and Vauchez, A., 2008. Feedback between melt percolation and
1065 deformation in an exhumed lithosphere-asthenosphere boundary. *Earth and Planetary Science Letters*,
1066 274, 401-413, doi: 10.1016/j.epsl.2008.07.053.
1067
1068 Liang, Y., Schiemenz, A., Hesse, M.A. and Parmentier, E.M., 2011. Waves, channels, and the
1069 preservation of chemical heterogeneities during melt migration in the mantle. *Geophysical Research*
1070 *Letters*, 38, L20308, doi: 10.1029/2011GL049034.
1071
1072 Lissenberg, J.C., Dick, H.J.B., 2008. Melt-rock reaction in the lower oceanic crust and its
1073 implications for the genesis of mid-ocean ridge basalt. *Earth and Planetary Science Letters*, 271, 311-
1074 325, doi: 10.1016/j.epsl.2008.04.023.
1075
1076 Lissenberg, C.J., MacLeod, C.J., Howard, K.A. and Godard, M., 2013. Pervasive reactive
1077 melt migration through fast-spreading lower oceanic crust (Hess Deep, equatorial Pacific Ocean).
1078 *Earth and Planetary Science Letters*, 361, 436-447, doi: 10.1016/j.epsl.2012.11.012.
1079

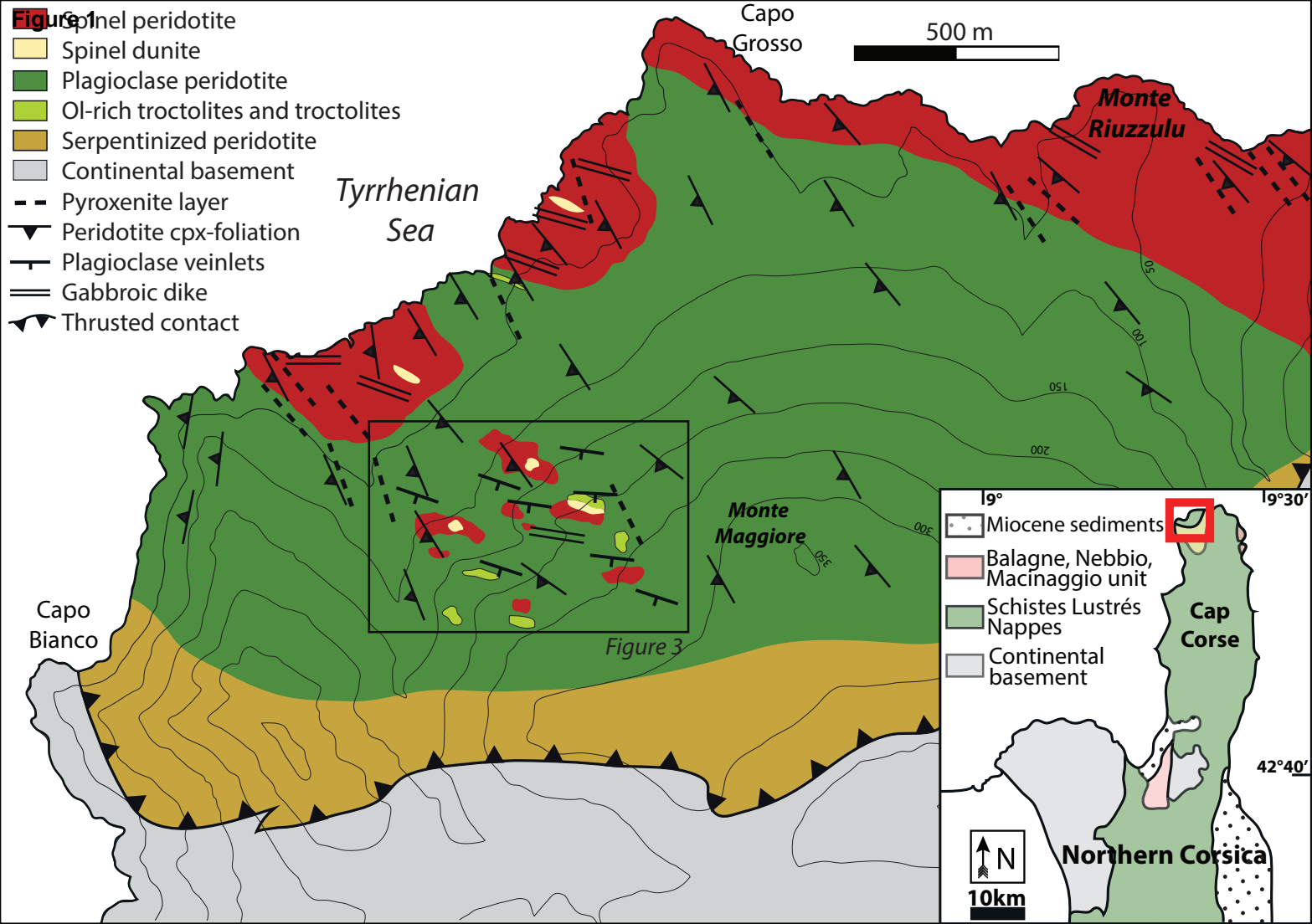
1080 Mainprice, D., Tommasi, A., Couvy, H., Cordier, P. and Frost, D.J., 2005. Pressure sensitivity
1081 of olivine slip systems and seismic anisotropy of Earth's upper mantle. *Nature*, 433, 731-733, doi:
1082 10.1038/nature03266.
1083
1084 Mainprice, D., Bachmann, F., Hielscher, R., Schaeben, H., 2014. Descriptive tools for the
1085 analysis of texture projects with large datasets using MTEX: strength, symmetry and components.
1086 *Geological Society of London, Special Publications*, 409, doi: 10.1144/SP1409.1148.
1087
1088 Manatschal, G. and Müntener, O., 2009. A type sequence across an ancient magma-poor
1089 ocean-continent transition: the example of the western Alpine Tethys ophiolites. *Tectonophysics*, 473,
1090 4-19, doi: 10.1016/j.tecto.2008.07.021.
1091
1092 Müntener, O. and Piccardo, G.B., 2003. Melt migration in ophiolitic peridotites: the message
1093 from Alpine–Apennine peridotites and implications for embryonic ocean basin. In: Dilek, Y.,
1094 Robinson, P.T. (Eds.), *Ophiolites in Earth History: Geological Society of London Special Publication*,
1095 218, 69–89, doi: 0305-8719/03.
1096
1097 Müntener, O., Pettke, T., Desmurs, L., Meier, M. and Schaltegger, U., 2004. Refertilization of
1098 mantle peridotite in embryonic ocean basins: trace element and Nd isotopic evidence and implications
1099 for crust-mantle relationships. *Earth and Planetary Science Letters*, 221, 293-308, doi:
1100 10.1016/S0012-821X(04)00073-1.
1101
1102 Paquet, M., Cannat, M., Brunelli, D., Hamelin, C. and Humler, E., 2016. Effect of
1103 melt/mantle interactions on MORB chemistry at the easternmost Southwest Indian Ridge (61 to
1104 67°E). *Geochemistry, Geophysics, Geosystems*, 17, 4605-4640, doi: 10.1002/2016GC006385.
1105
1106 Pearce, N. J. G., Perkins, W. T., Westgate, J. a., Gorton, M. P., Jackson, S. E., Neal, C. R. and
1107 Chenery, S. P., 1997. A Compilation of New and Published Major and Trace Element Data for NIST
1108 SRM 610 and NIST SRM 612 Glass Reference Materials. *Geostandards and Geoanalytical Research*,
1109 21, 115–144, doi: 10.1111/j.1751-908X.1997.tb00538.x.
1110
1111 Piccardo, G.B., Müntener, O., Zanetti, A., Romairone, A., Bruzzone, S., Poggi, E. and
1112 Spagnolo, A., 2004. The Lanzo south peridotite: Melt/peridotite interaction in the mantle lithosphere
1113 of the Jurassic Ligurian Tethys. *Ophioliti*, 29, 37-62, doi: 10.4454/ofioliti.v29i1.205.
1114
1115 Piccardo, G.B. and Vissers, R.L.M., 2007. The pre-oceanic evolution of the Erro-Tobbio
1116 peridotite (Voltri Massif - Ligurian Alps, Italy). *Journal of Geodynamics*, 43, 417–449, doi:
1117 10.1016/j.jog.2006.11.001.
1118
1119 Piccardo, G.B., Zanetti, A. and Müntener, O., 2007. Melt/peridotite interaction in the
1120 Southern Lanzo peridotite: Field, textural and geochemical evidence. *Lithos*, 94, 181-209, doi:
1121 10.1016/j.lithos.2006.07.002.
1122
1123 Piccardo, G.B., Guarnieri, L., 2010. The Monte Maggiore peridotite (Corsica, France): a case
1124 study of mantle evolution in the Ligurian Tethys. *Geological Society of London*, 337, 7-45, doi:
1125 10.1144/SP337.2 0305-8719/10.
1126

1127 Pirard, C., Hermann, J. and O'Neill, H.S.T.C., 2013. Petrology and geochemistry of the Crust-
1128 Mantle boundary in a nascent arc, Massif du Sud ophiolite, New Caledonia, SW Pacific. *Journal of*
1129 *Petrology*, 54, 1759-1792, doi: 10.1093/petrology/egt030.
1130
1131 Rampone, E., Piccardo, G.B., Vannucci, R. and Bottazzi, P., 1997. Chemistry and origin of
1132 trapped melts in ophiolitic peridotites. *Geochimica et Cosmochimica Acta*, 21, 4557-4569, doi: 0016-
1133 7037/97.
1134
1135 Rampone, E. and Piccardo, G.B., 2000. The ophiolite-oceanic lithosphere analogue: new
1136 insights from the Northern Apennines (Italy). In: Dilek Y, Moores EM, Elthon D, Nicolas A (eds)
1137 *Ophiolites and oceanic crust: new insights from field studies and the oceanic drilling program.*
1138 *Geological Society of America Special Paper*, Boulder, 349, 21-34, doi: 10.1130/0-8137-2349-3.21.
1139
1140 Rampone, E., Borghini, G., 2008. Melt migration and intrusion in the Erro-Tobbio peridotites
1141 (Ligurian Alps, Italy): Insights on magmatic processes in extending lithospheric mantle. *European*
1142 *Journal of Mineralogy*, 20, 573-585, doi: 10.1127/0935-1221/2008/0020-1807.
1143
1144 Rampone, E., Romairone, A. and Hofmann, A.W., 2004. Contrasting bulk and mineral
1145 chemistry in depleted mantle peridotites: evidence for reactive porous flow. *Earth and Planetary*
1146 *Science Letters*, 2018, 491-506, doi: 10.1016/S0012-821X(03)00679-4.
1147
1148 Rampone, E., Piccardo, G.B. and Hofmann, A.W., 2008. Multi-stage melt-rock interaction in
1149 the Mt. Maggiore (Corsica, France) ophiolitic peridotites: microstructural and geochemical evidence.
1150 *Contributions to Mineralogy and Petrology*, 156, 453-475. doi: 10.1007/s00410-008-0296-y.
1151
1152 Rampone, E., Borghini, G., Godard, M., Ildefonse, B., Crispini, L. And Fumagalli, P., 2016.
1153 Melt/rock reaction at oceanic peridotite/gabbro transition as revealed by trace element chemistry of
1154 olivine. *Geochimica et Cosmochimica Acta*, 190, 309-331, doi: 10.1016/j.gca.2016.06.029.
1155
1156 Renna, M.R., Tribuzio, R., 2011. Olivine-rich troctolites from Ligurian ophiolites (Italy):
1157 Evidence for impregnation of replacive mantle conduits by MORB-type melts. *Journal of Petrology*,
1158 52, 1763-1790, doi: 10.1093/petrology/egr029.
1159
1160 Renna, M.R., Tribuzio, R. and Ottolini, L., 2016. New perspectives on the origin of olivine-
1161 rich troctolites and associated harrisites from the Ligurian ophiolites (Italy). *Journal of the Geological*
1162 *Society*, 174, doi: 10.1144/jgs2015-135.
1163
1164 Rosenberg, C.L. and Handy, M.R., 2005. Experimental deformation of partially melted
1165 granite revisited: implications for the continental crust. *Journal of Metamorphic Geology*, 23, 19-28,
1166 doi: 10.1111/j.1525-1314.2005.00555.x.
1167
1168 Sanfilippo, A. and Tribuzio, R., 2012. Building of the deepest crust at a fossil slow-spreading
1169 centre (Pineto gabbroic sequence, Alpine Jurassic ophiolites). *Contributions to Mineralogy and*
1170 *Petrology*, 165, 705-721, doi: 10.1007/s00410-012-0831-8.
1171
1172 Sanfilippo, A., Dick, H.J.B. and Ohara, Y., 2013. Melt-rock reaction in the Mantle: Mantle
1173 troctolites from the Parece Vela ancient back-arc spreading center. *Journal of Petrology*, 54, 861-885,
1174 doi: 10.1093/petrology/egs089.

1175
1176 Sanfilippo, A., Tribuzio, R. and Tiepolo, M., 2014. Mantle-crust interactions in the oceanic
1177 lithosphere: Constraints from minor and trace elements in olivine. *Geochimica et Cosmochimica*
1178 *Acta*, 141, 423-439, doi: 10.1016/j.gca.2014.06.012.
1179
1180 Sanfilippo, A., Morishita, T., Kumagai, H., Nakamura, K., Okino, K., Hara, K., Tamura, A.
1181 and Arai, S., 2015. Hybrid troctolites from Mid-Ocean Ridges: Inherited mantle in the lower crust,
1182 *Lithos*, 232, 124-130, doi: 10.1016/j.lithos.2015.06.025
1183
1184 Sanfilippo, A., Dick, H.J.B., Ohara, Y. and Tiepolo, M., 2016. New insights on the origin of
1185 troctolites from the breakaway area of the Godzilla Megamullion (Parece Vela back-arc basin): The
1186 role of melt-mantle interaction on the composition of the lower crust. *Island arc*, 25, 220-234, doi:
1187 10.1111/iar.12137.
1188
1189 Sanfilippo, A., Tribuzio, R., Ottolini, L. and Hamada, M., 2017. Water, lithium and trace
1190 element compositions of olivine from Lanzo South replacive mantle dunites (Western Alps): New
1191 constraints into melt migration processes at cold thermal regimes. *Geochimica et Cosmochimica Acta*,
1192 214, 51-72, doi: 10.1016/j.gca.2017.07.034.
1193
1194 Saper, L., Liang, Y., 2014. Formation of plagioclase-bearing peridotite and plagioclase-
1195 bearing wehrlite and gabbro suite through reactive crystallization: an experimental study.
1196 *Contributions to Mineralogy and Petrology*, 167, 985, doi: 10.1007/s00410-014-0985-7.
1197
1198 Seyler, M., Lorand, J.P., Dick, H.J.B. and Drouin, M., 2007. Pervasive melt percolation
1199 reactions in ultra-depleted refractory harzburgites at the Mid-Atlantic Ridge, 15°20'N: ODP Hole
1200 1274A. *Contributions to Mineralogy and Petrology*, 153, 303, doi: 10.1007/s00410-006-0148-6.
1201
1202 Soustelle, V., Tommasi, A., Bodinier, J.L., Garrido, C.J. and Vauchez, A., 2009. Deformation
1203 and reactive melt transport in the mantle lithosphere above a large-scale partial melting domain : the
1204 Ronda peridotite massif, Southern Spain. *Journal of Petrology*, 50, 1235-1266, doi:
1205 10.1093/petrology/egp032.
1206
1207 Soustelle, V., Tommasi, A., Demouchy, S. and Ionov, D.A., 2010. Deformation and fluid-
1208 rock interaction in the supra-subduction mantle: microstructures and water contents in peridotite
1209 xenoliths from the Avacha volcano, Kamchatka. *Journal of Petrology*, 51, 363-394, doi:
1210 10.1093/petrology/egp085.
1211
1212 Soustelle, V., Walte, N.P., Geeth, M.A., Manthilake, M. and Frost, D.J., 2014. Melt migration
1213 and melt-rock reactions in the deforming Earth's upper mantle: Experiments at high pressure and
1214 temperature. *Geology*, 42, 83-86, doi: 10.1130/G34889.1.
1215
1216 Spiegelman, M. and Kelemen, P.B., 2003. Extreme chemical variability as a consequence of
1217 channelized melt transport. *Geochemistry, Geophysics, Geosystems*, 4, 1055-1072, doi:
1218 10.1029/2002GC000336.
1219
1220 Suhr, G., Hellebrand, E., Johnson, K. and Brunelli, D., 2008. Stacked gabbro units and
1221 intervening mantle: A detailed look at a section of IODP Leg 305, Hole U1309D. *Geochemistry,*
1222 *Geophysics, Geosystems*, 9, Q10007, doi: 10.1029/2008GC002012.

1223
1224 Sun, S.S., McDonough, W.F., 1989. Chemical and isotopic systematics of oceanic basalts:
1225 implications for mantle composition and processes. Geological Society of London, Special
1226 Publications, 42, 313-345, doi: 10.1144/GSL.SP.1989.042.01.19.
1227
1228 Sun, C., Liang, Y., 2012. Distribution of REE between clinopyroxene and basaltic melt along
1229 a mantle adiabat: effects of major element composition, water and temperature. Contributions to
1230 Mineralogy and Petrology, 163, 807-823, doi: 10.1007/s00410-011-0700-x.
1231
1232 Sun, C., Liang, Y., 2013a. The importance of crystal chemistry on REE partitioning between
1233 mantle minerals (garnet, clinopyroxene, orthopyroxene, and olivine) and basaltic melts. Chemical
1234 Geology, 358, 23-36, doi: 10.1016/j.chemgeo.2013.08.045.
1235
1236 Sun, C., Liang, Y., 2013b. Distribution of REE and HFSE between low-Ca pyroxene and
1237 lunar picritic glass melts around multiple saturation points. Geochimica et Cosmochimica Acta, 119,
1238 340-358, doi: 10.1016/j.gca.2013.05.036.
1239
1240 Sun, C., Liang, Y., 2014. An assessment of subsolidus re-equilibration on REE distribution
1241 among mantle minerals olivine, orthopyroxene, clinopyroxene, and garnet in peridotites. Chemical
1242 Geology, 372, 80-91, doi: 10.1016/j.chemgeo.2014.02.014.
1243
1244 Tommasi, A., Tikoff, B. and Vauchez, A., 1999. Upper mantle tectonics: three-dimensional
1245 deformation, olivine crystallographic fabrics and seismic properties. Earth and Planetary Science
1246 Letters, 168, 173-186, doi: 10.1016/S0012-821X(99)00046-1.
1247
1248 Tommasi, A., Mainprice, D., Canova, G., Chastel, Y., 2000. Viscoplastic self-consistent and
1249 equilibrium-based modeling of olivine lattice preferred orientations: Implications for the upper mantle
1250 seismic anisotropy. Journal of Geophysical Research, 105, 7893-7908, doi: 10.1029/1999JB900411.
1251
1252 Tommasi, A., Godard, M., Coromina, G., Dautria, J.M. and Barszczus, H., 2004. Seismic
1253 anisotropy and compositionally induced velocity anomalies in the lithosphere above mantle plumes: A
1254 petrological and microstructural study of mantle xenoliths from French Polynesia. Earth and Planetary
1255 Science Letters, 227, 539-556, doi: 10.1016/j.epsl.2004.09.019.
1256
1257 Tommasi, A., Vauchez, A. and Ionov, D.A., 2008. Deformation, static recrystallization, and
1258 reactive melt transport in shallow subcontinental mantle xenoliths (Tok Cenozoic volcanic field, SE
1259 Siberia). Earth and Planetary Science Letters, 272, 65-77, doi: 10.1016/j.epsl.2008.04.020.
1260
1261 Tursack, E., Liang, Y., 2012. A comparative study of melt-rock reactions in the mantle:
1262 laboratory dissolution experiments and geological field observations. Contributions to Mineralogy and
1263 Petrology, 163, 861-876, doi: 10.1007/s00410-011-0703-7.
1264
1265 Van Achterberg E., Griffin W.L. and Stiefenhofer J., 2001. Metasomatism in mantle xenoliths
1266 from the Letlhakane kimberlites: estimation of element fluxes. Contribution to Mineralogy and
1267 Petrology, 141, 397– 414, doi: 10.1007/s004100000236.
1268
1269 Van den Bleeken, G., Müntener, O., Ulmer, P., 2011. Melt variability in percolated
1270 peridotite: an experimental study applied to reactive migration of tholeiitic basalt in the upper

1271 mantle. *Contribution to Mineralogy and Petrology*, 161, 921-945, doi: 10.1007/s00410-010-0572-
1272 5.
1273
1274 Vernières, L., Godard, M. and Bodinier, J.L., 1997. A plate model for the simulation of trace
1275 element fractionation during partial melting and magma transport in the Earth's upper mantle. *Journal*
1276 *of Geophysical Research*, 102, 24771-24784, doi: 10.1029/97JB1946.
1277
1278 Warren, J.M., 2016. Global variations in Abyssal Peridotite Compositions. *Lithos*, 248-251,
1279 193-219, doi: 10.1016/j.lithos.2015.12.023.
1280
1281 Workman, R.K. and Hart, S.R., 2005. Major and trace element composition of the depleted
1282 MORB mantle (DMM). *Earth and Planetary Science Letters*, 231, 53-72, doi:
1283 10.1016/j.epsl.2004.12.005.



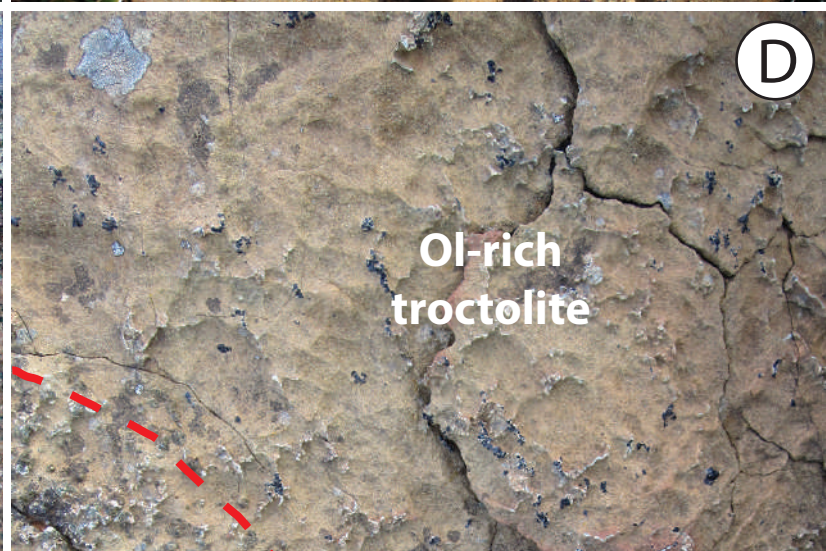
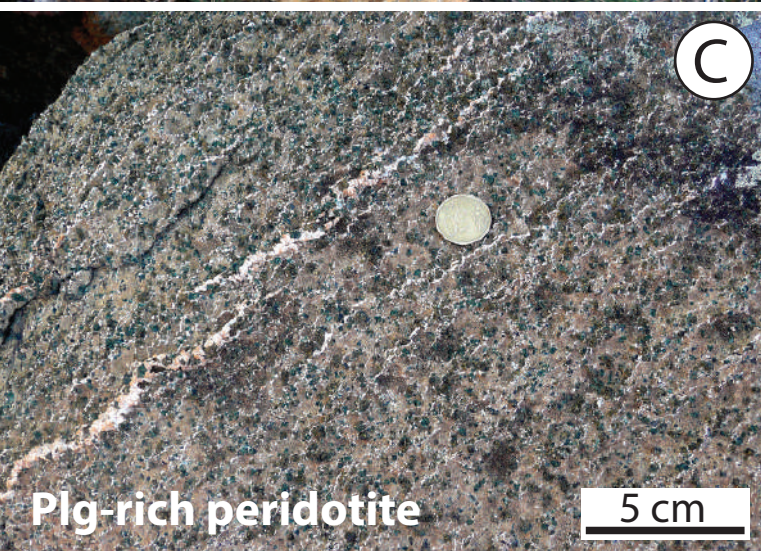
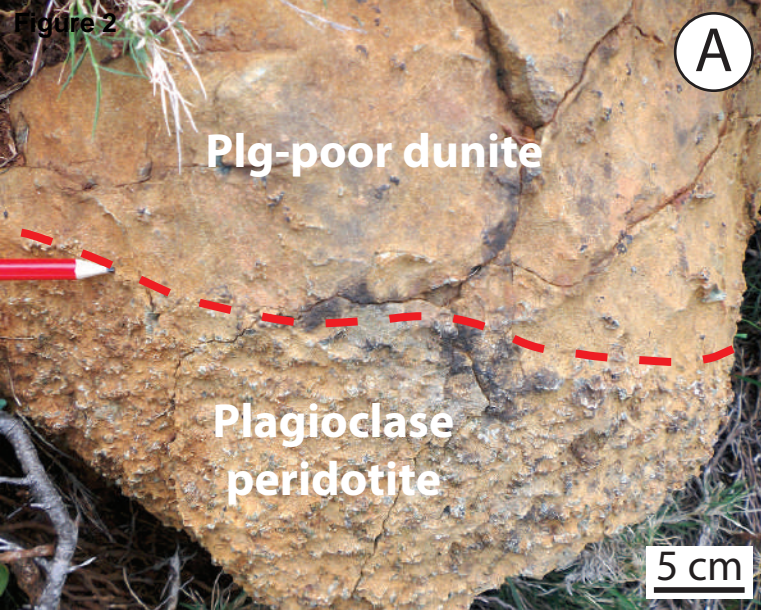


Figure 3

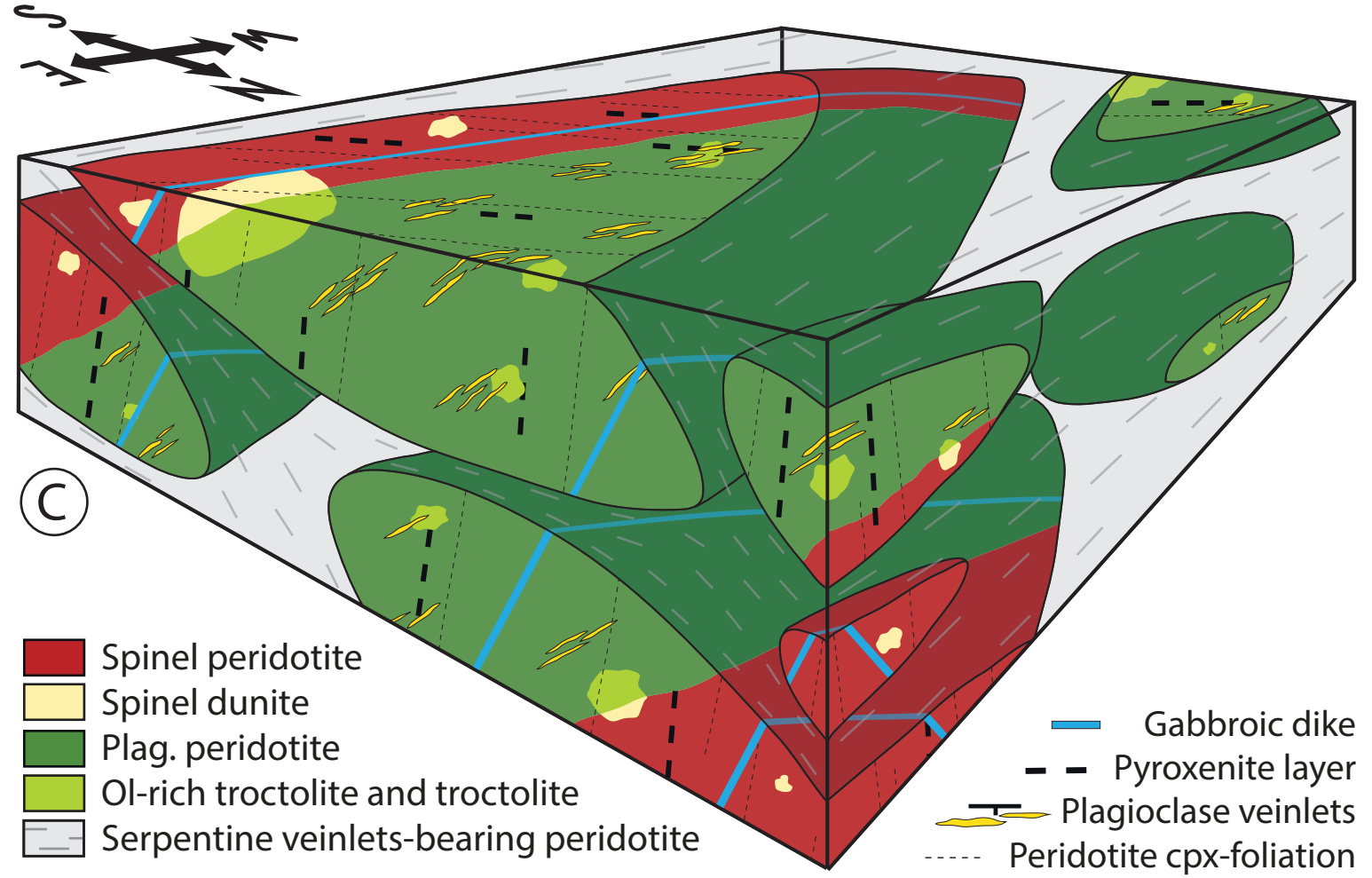
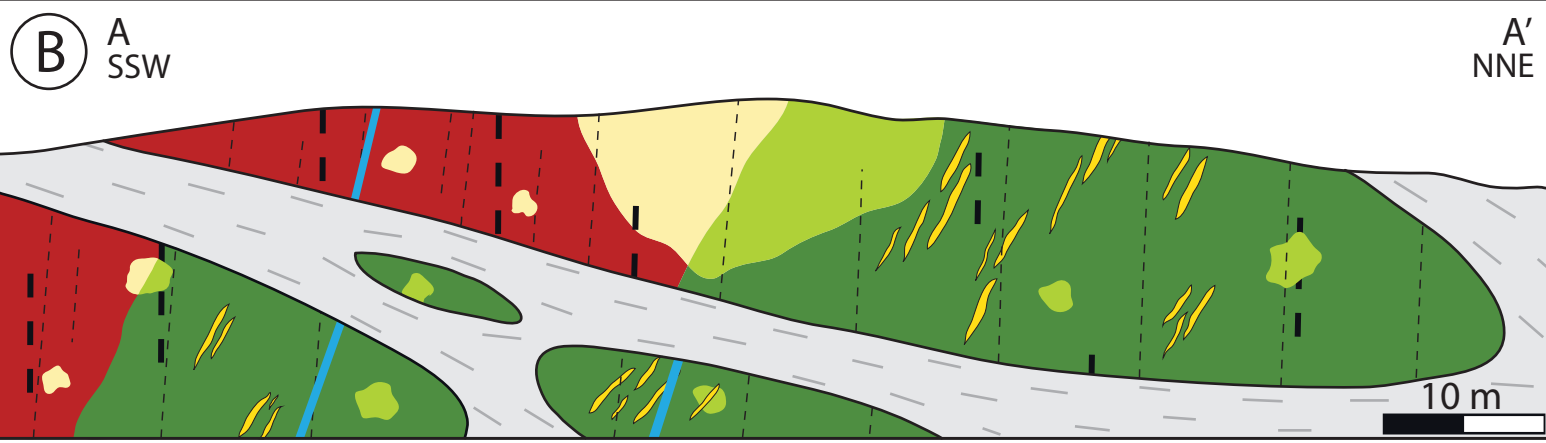
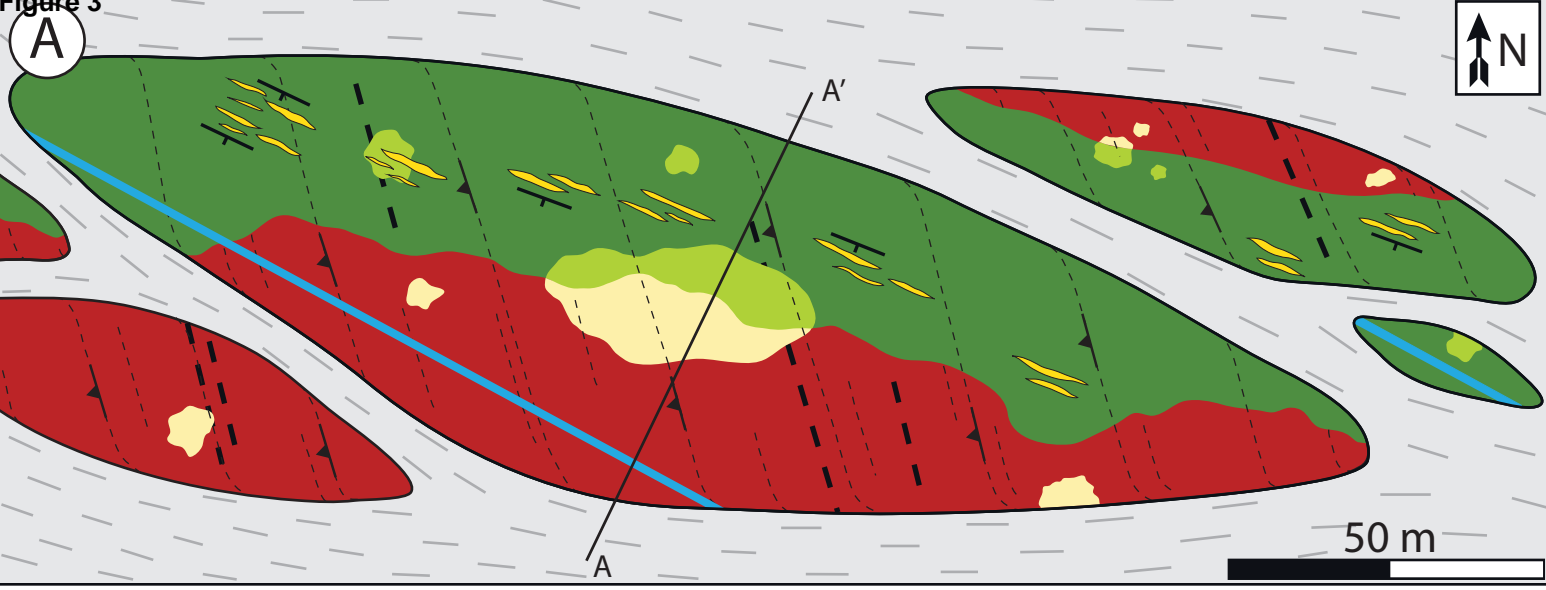


Figure 4

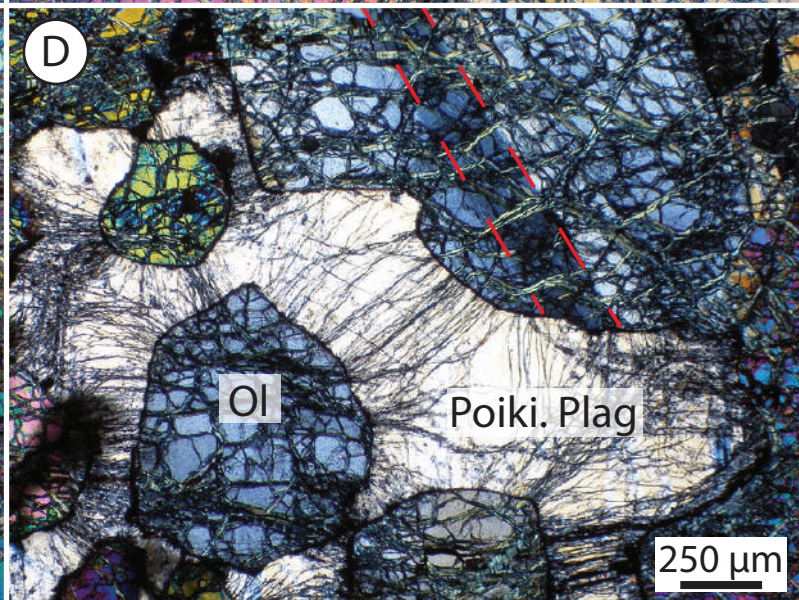
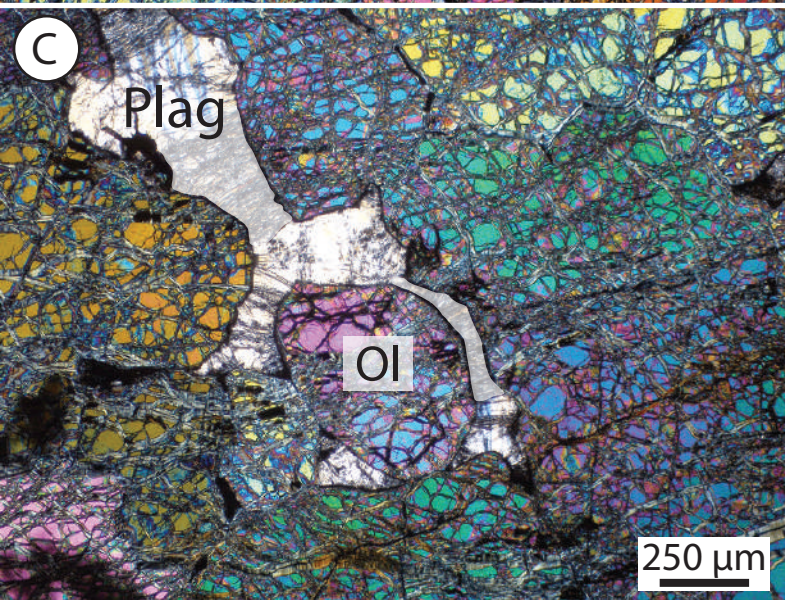
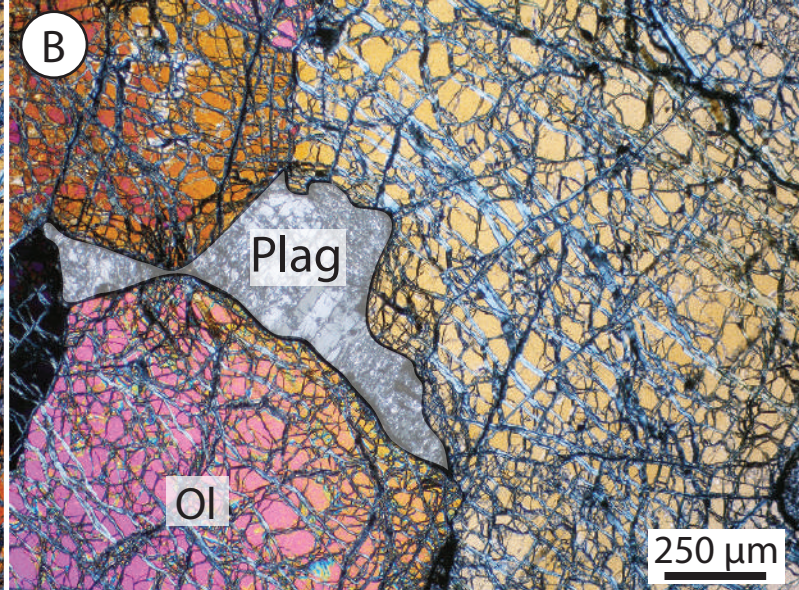
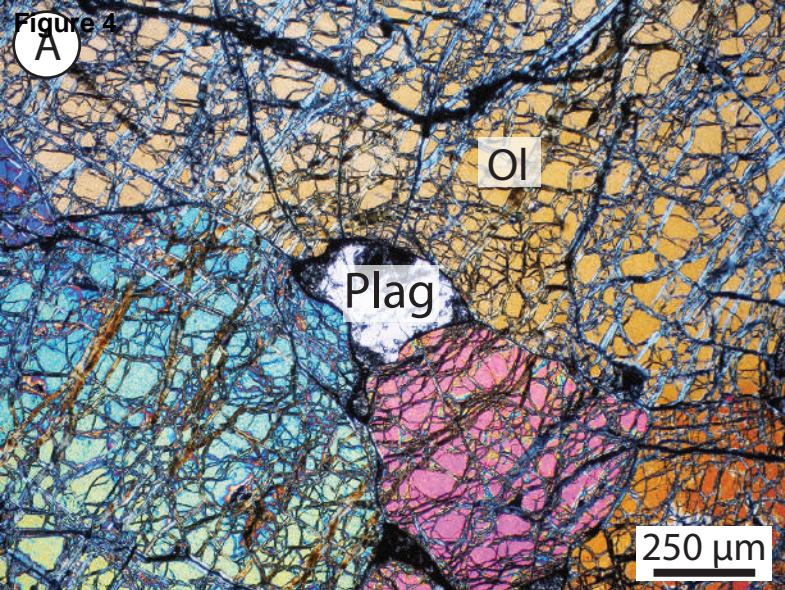


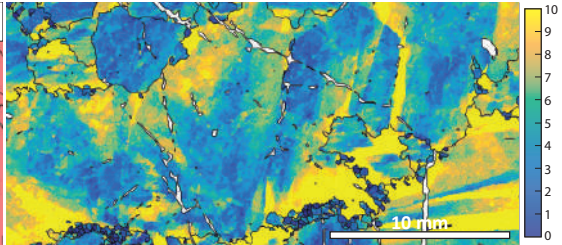
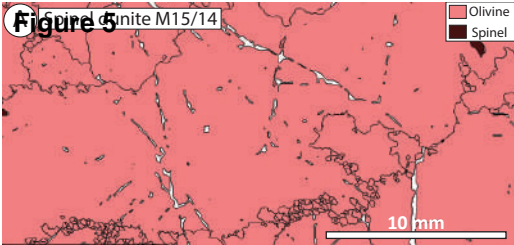
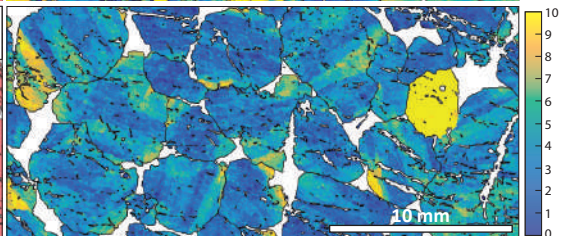
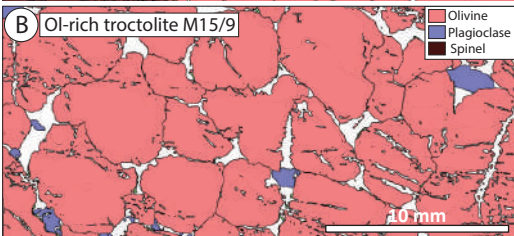
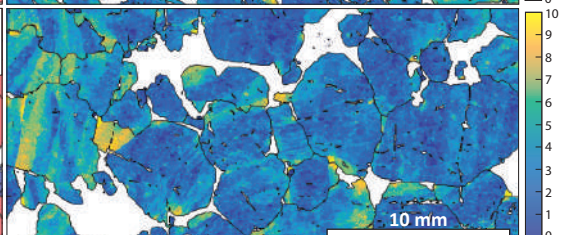
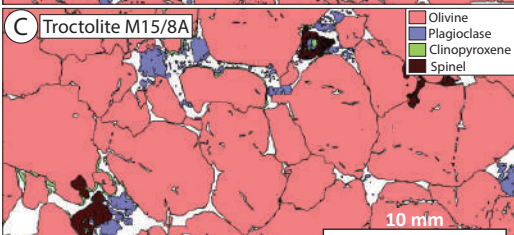
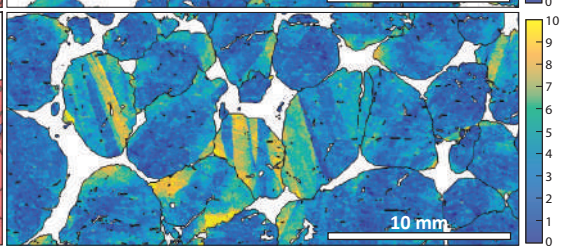
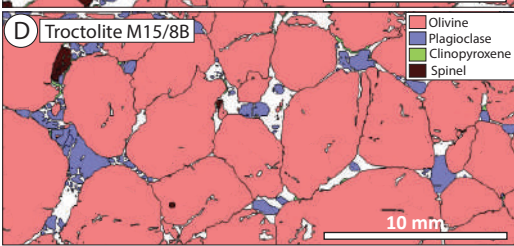
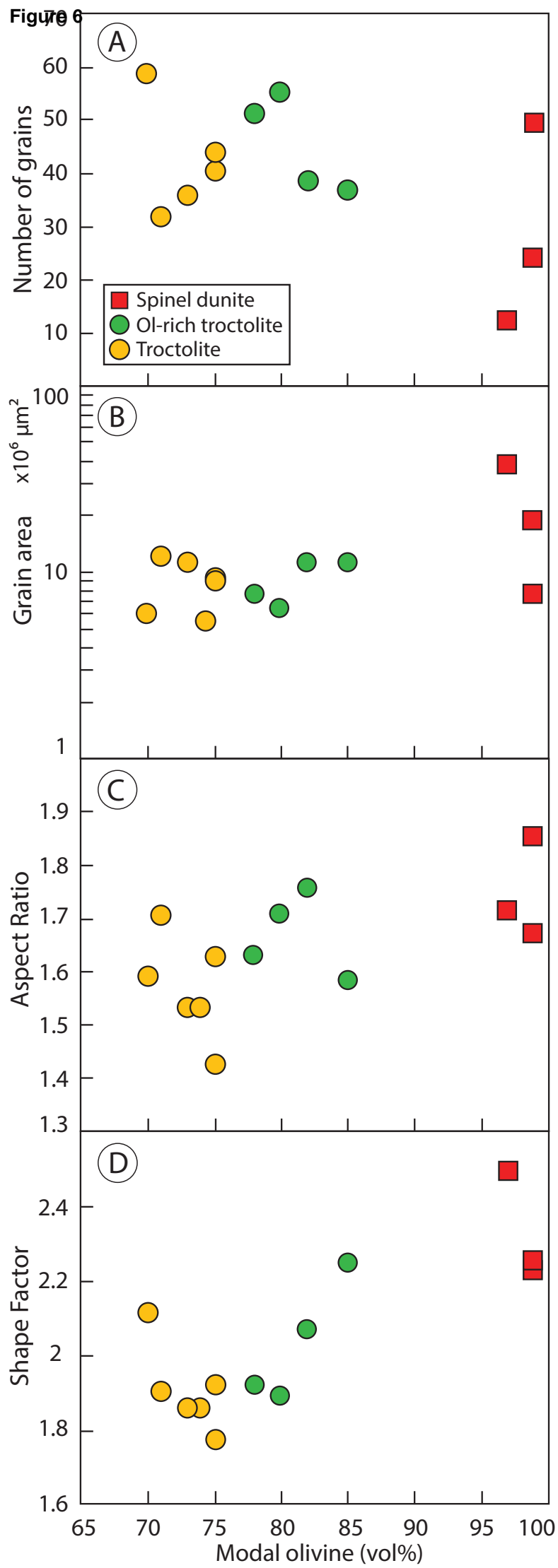
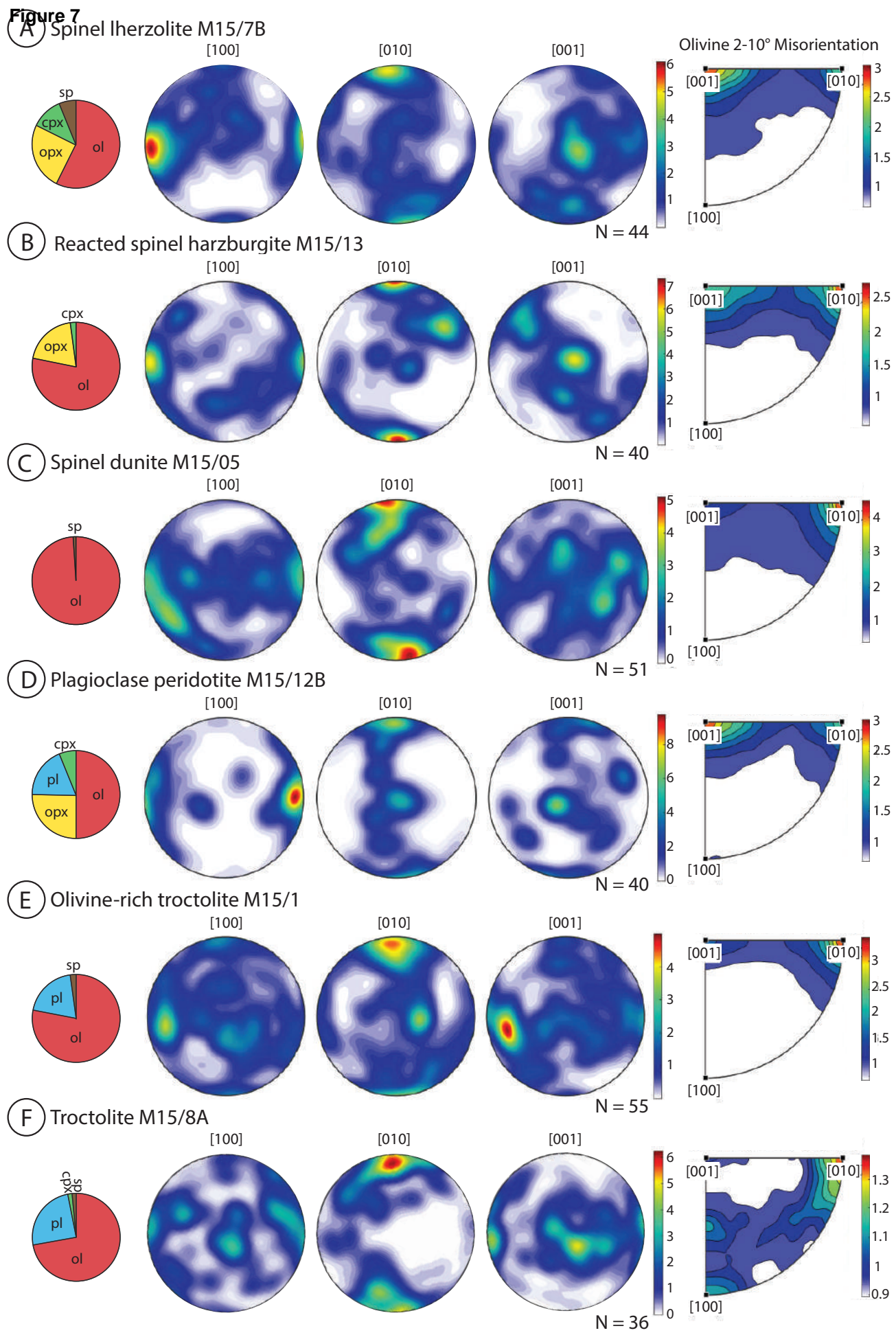
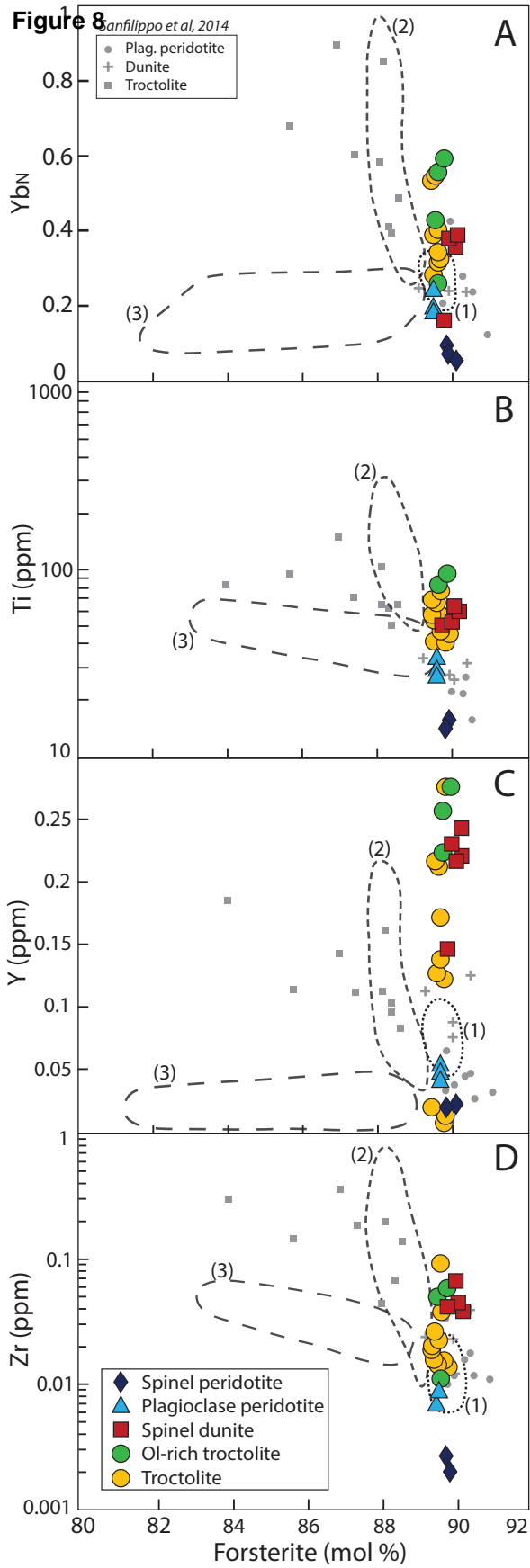
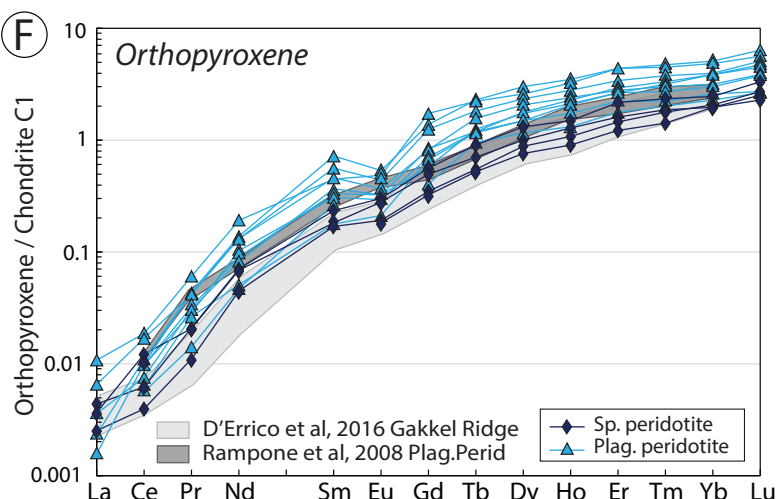
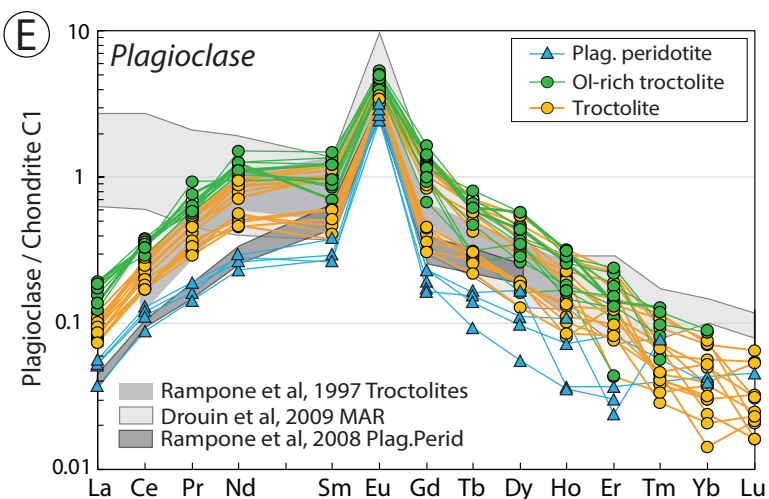
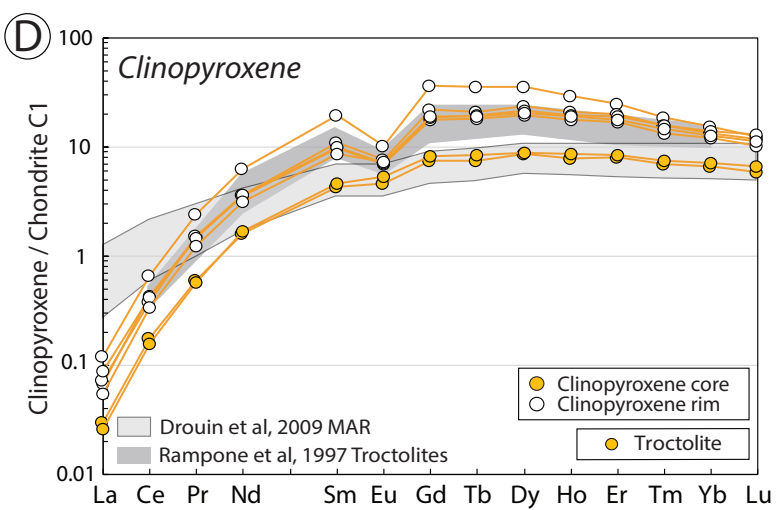
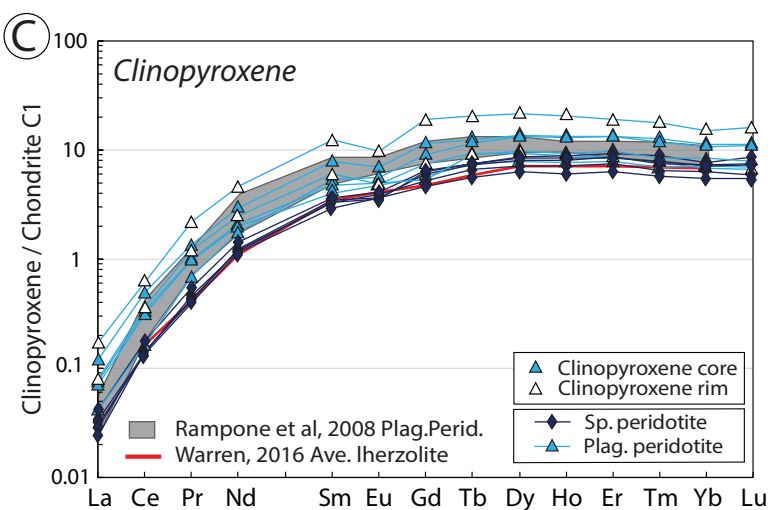
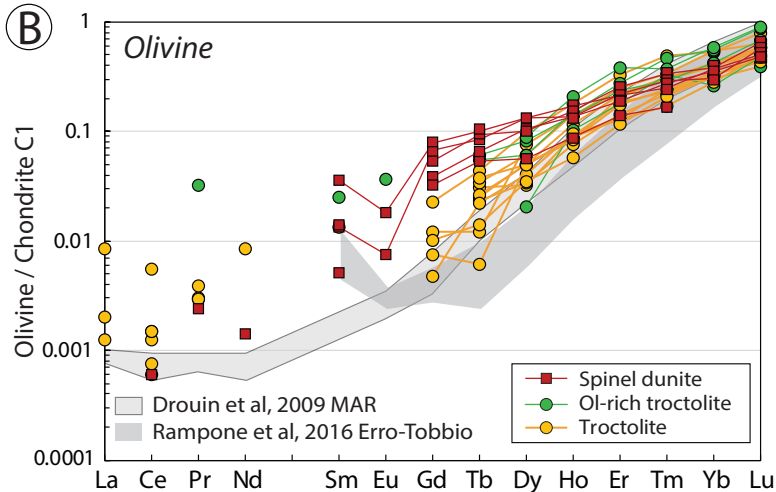
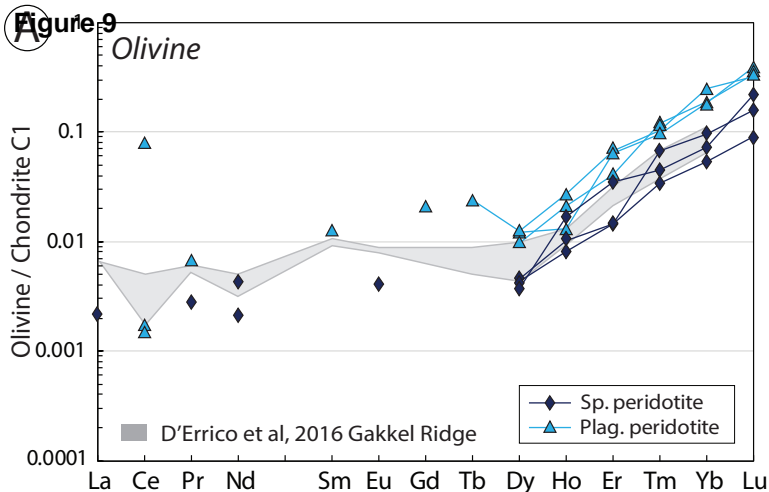
Figure 5 Spine M15/14**B** Ol-rich troctolite M15/9**C** Troctolite M15/8A**D** Troctolite M15/8B

Figure 6









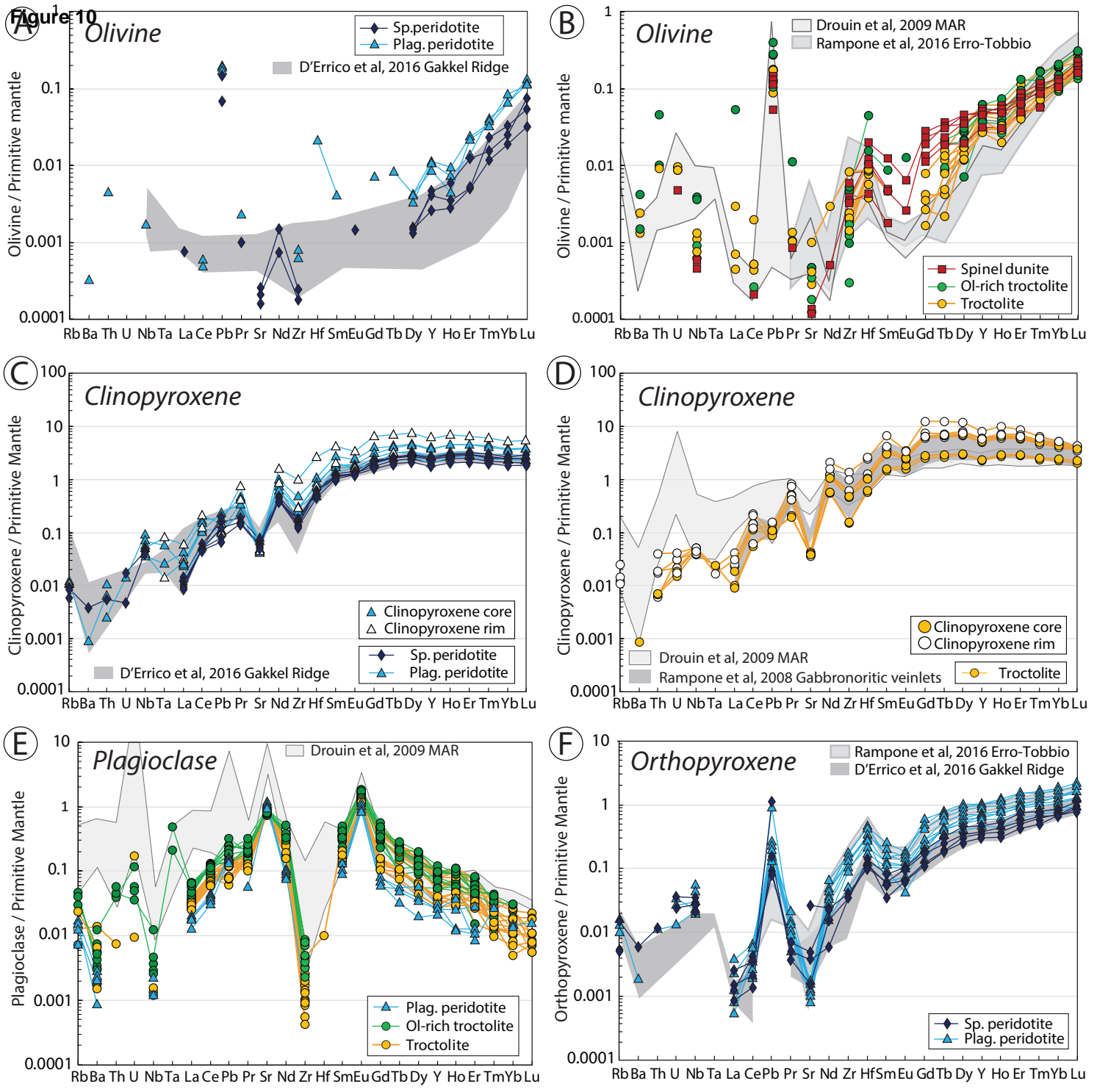


Figure 11

Reactive melt percolation - Spinel facies

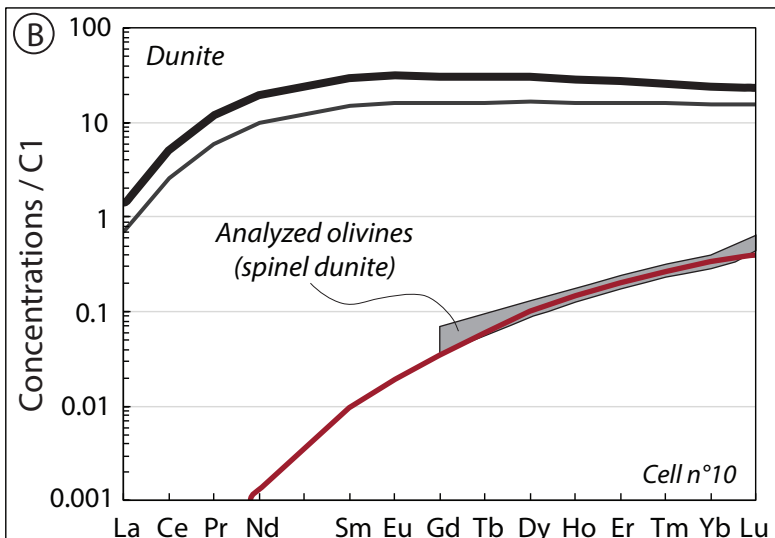
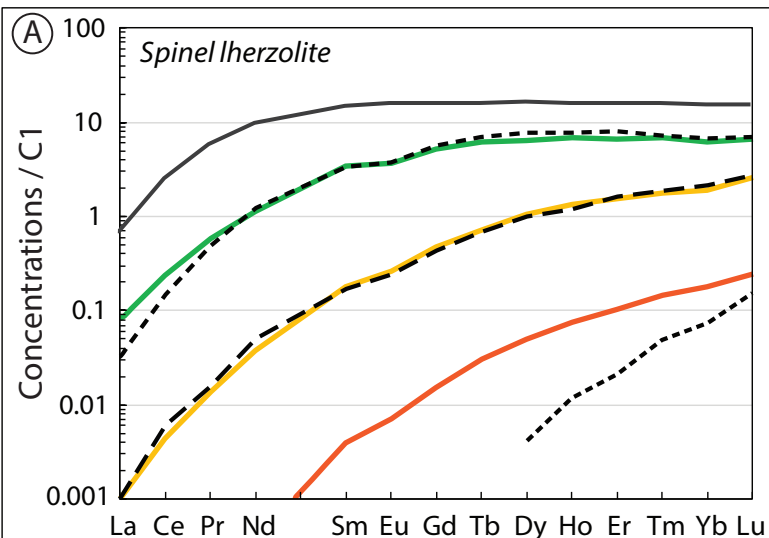
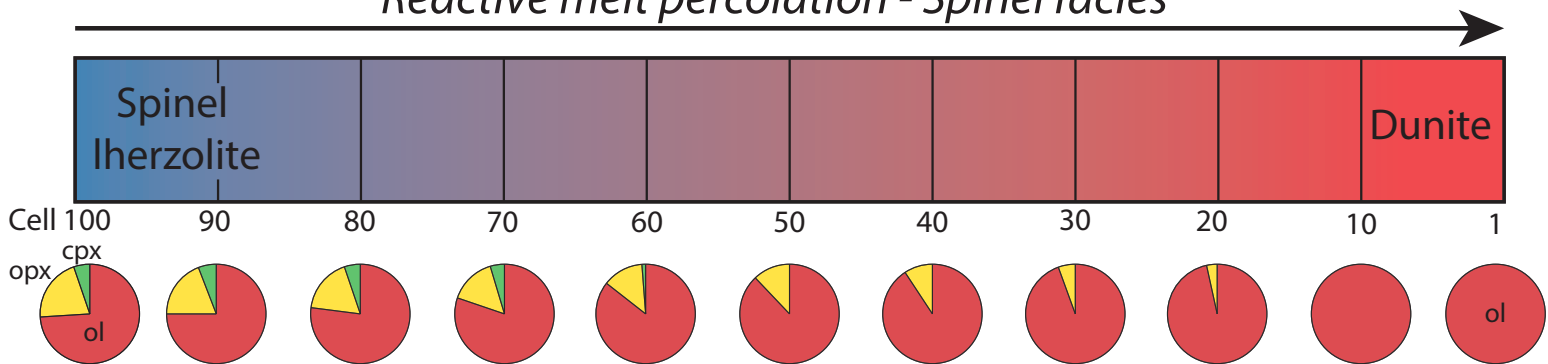


Figure 12

Melt impregnation - Plagioclase facies

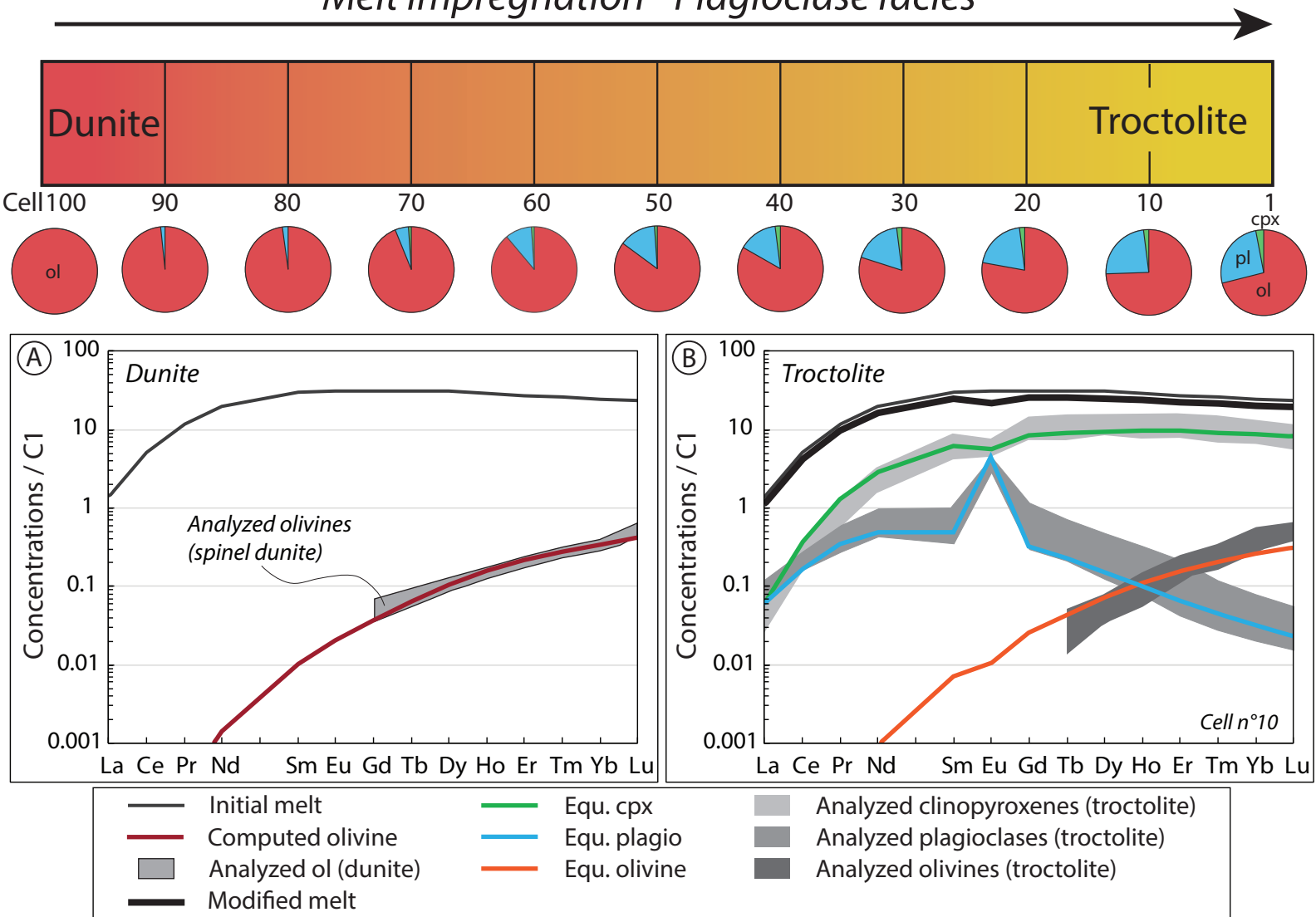


Figure 13

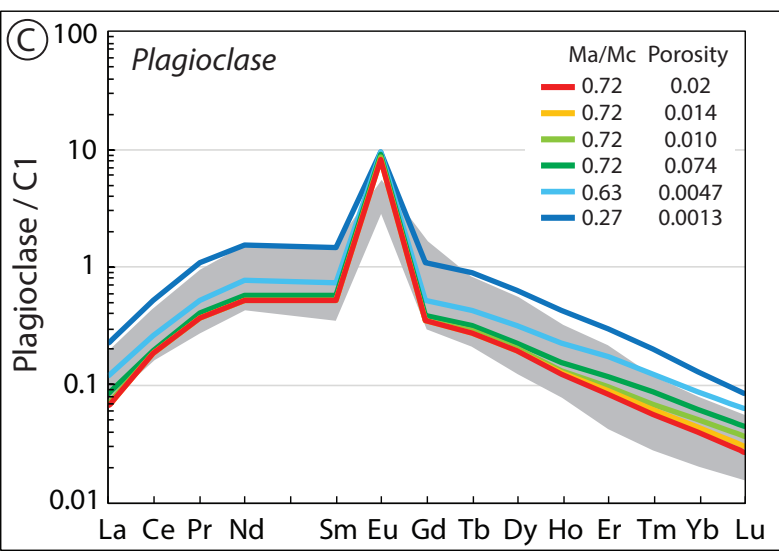
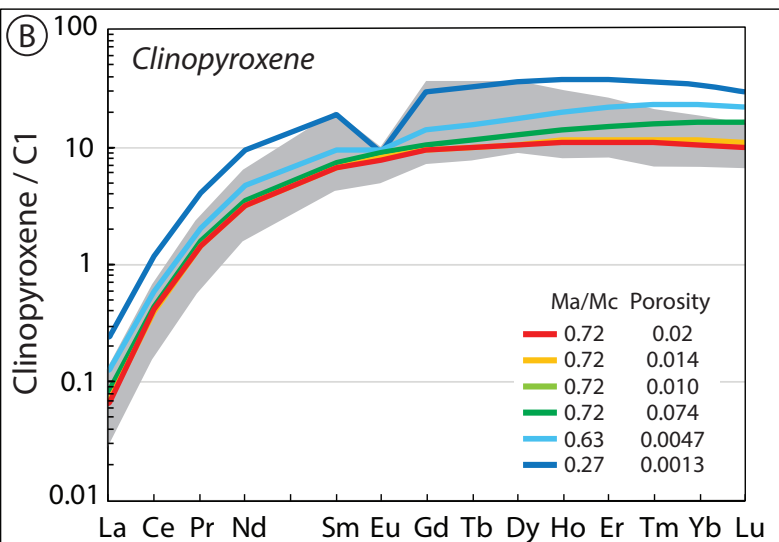
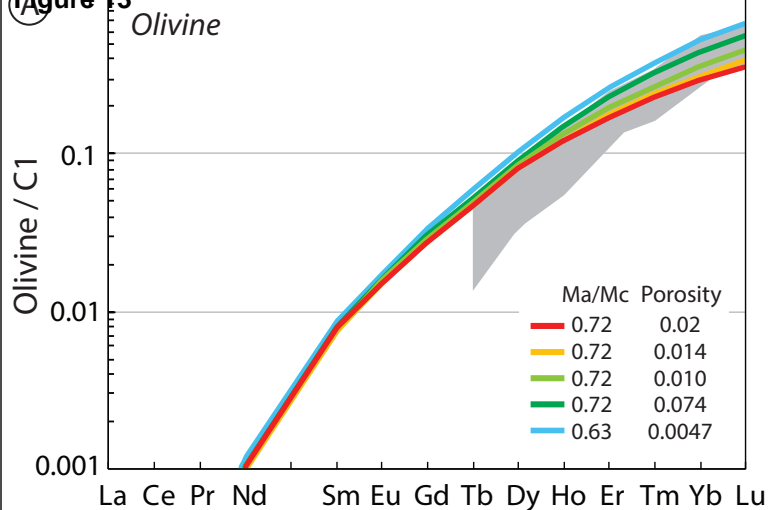
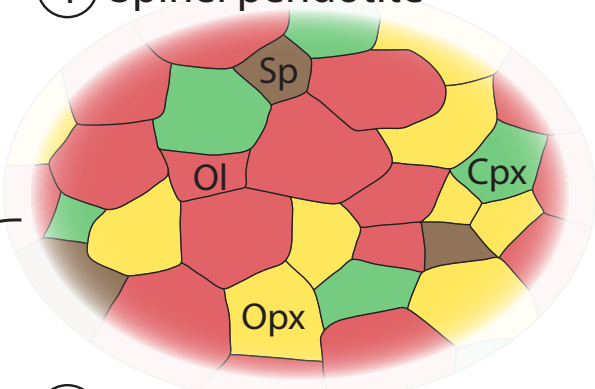
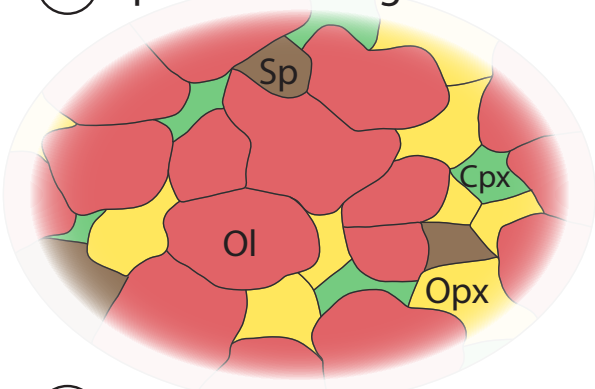


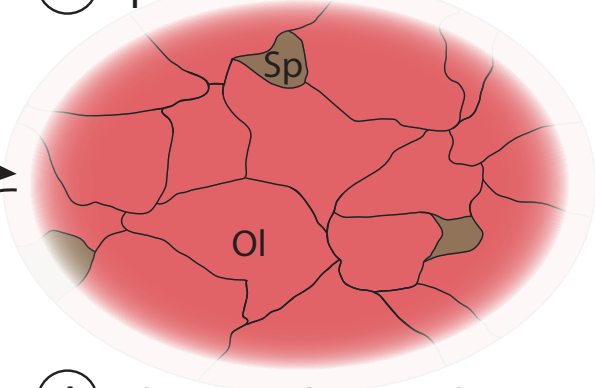
Figure 14 (1) Spinel peridotite



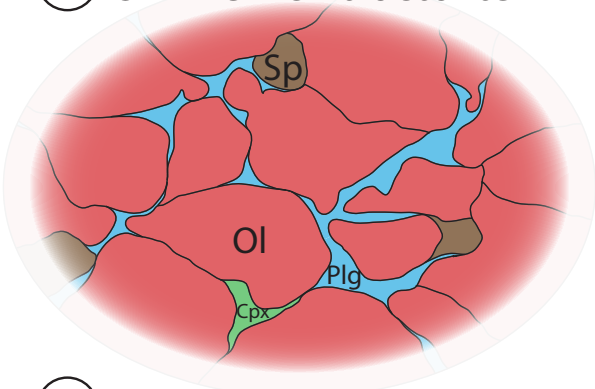
(2) Spinel harzburgite



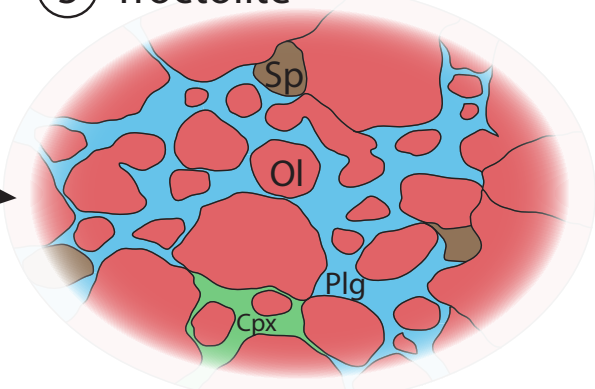
(3) Spinel dunite



(4) Olivine-rich troctolite



(5) Troctolite



Reactive porous flow

Impregnation

Table 1[Click here to download Table: Table 1 Analyzed samples.docx](#)

Sample	Lithotype	Modal composition					Textural parameters			
		Olivine	Plagio	Cpx	Opx	Spinel	N° Grains	Grain area (µm ²)	Aspect Ratio	Shape Factor
M15/7	Sp. lherzolite	58	0	11	25	6	63	3.81E+06	1.64	2.46
M15/7B	Sp. lherzolite	62	0	13	23	2	44	8.04E+06	1.64	2.64
M15/13	Sp. harzburgite	78	0	2	20	0	40	8.47E+06	1.73	2.35
M15/15	Plag. lherzolite	74	0	10	15	1	42	9.71E+06	1.67	1.82
M15/12B	Plag. harzburgite	65	8	8	18	1	40	7.44E+06	1.69	2.29
M15/20A	Plag. harzburgite	58	17	1	24	0	28	6.21E+06	1.67	2.65
M15/18A	Plag. harzburgite	50	25	1	24	0	33	6.82E+06	1.52	2.04
M15/19	Plag. harzburgite	50	18	7	25	0	21	5.82E+06	1.56	2.19
M15/19B	Plag. harzburgite	48	15	6	31	0	37	5.73E+06	1.83	2.28
M15/3	Spinel dunite	97	0	0	0	3	12	3.81E+07	1.71	2.49
M15/5	Spinel dunite	99	0	0	0	1	51	6.54E+06	1.67	2.22
M15/14	Spinel dunite	99	0	0	0	1	24	1.91E+07	1.85	2.25
M15/9	Ol-rich troctolite	85	15	0	0	0	37	1.13E+07	1.59	2.24
M15/8A2	Ol-rich troctolite	82	17	0	0	1	39	1.13E+07	1.76	2.07
M15/1	Ol-rich troctolite	80	20	0	0	0	55	6.36E+06	1.71	1.89
M15/11	Ol-rich troctolite	78	20	0	0	2	51	7.58E+06	1.63	1.92
M15/8A3*	Troctolite	75	14	10	0	1	41	9.14E+06	1.43	1.92
M15/10A**	Troctolite	74	18	2	5	1	82	4.50E+06	1.54	1.86
M15/8B	Troctolite	73	25	1	0	1	44	9.25E+06	1.63	1.77
M15/8A	Troctolite	73	25	1	0	1	36	1.15E+07	1.54	1.86
M15/6	Troctolite	71	23	1	0	5	32	1.20E+07	1.71	1.91
M15/10B**	Troctolite	70	19	3	7	1	59	6.01E+06	1.59	2.11

Table 1: Studied samples, modal compositions and mean textural parameters of the olivine matrix.

* clinopyroxene-bearing troctolite

** sample at the contact between plagioclase peridotite and troctolite

Background dataset Figure S1

[Click here to download Background dataset for online publication only: Figure S1 MORB melt.pdf](#)

Background dataset Figure S2

[Click here to download Background dataset for online publication only: Figure S2 Ol-Cpx REE partitioning.pdf](#)

Background dataset Table S1

[Click here to download Background dataset for online publication only: Table S1 BIR1-G - Detection limit - Sensitivity.xlsx](#)

Background dataset Table S2

[Click here to download Background dataset for online publication only: Table S2 Mineral geochemistry - Olivine.xlsx](#)

Background dataset Table S3

[Click here to download Background dataset for online publication only: Table S3 Mineral geochemistry - Clinopyroxene.xlsx](#)

Background dataset Table S4

[Click here to download Background dataset for online publication only: Table S4 Mineral geochemistry - Plagioclase.xlsx](#)

Background dataset Table S5

[Click here to download Background dataset for online publication only: Table S5 Mineral geochemistry - Orthopyroxene.xlsx](#)

Background dataset Table S6

[Click here to download Background dataset for online publication only: Table S6 Standard deviation mineral geochemistry.xlsx](#)

Background dataset Table S7

[Click here to download Background dataset for online publication only: Table S7 Model parameters.xlsx](#)

Background dataset Methodologies

[Click here to download Background dataset for online publication only: Suppl.Mat. Methodologies.docx](#)